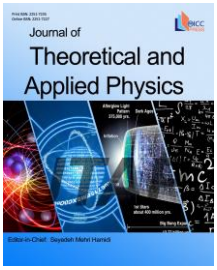

J. Theor. Appl. Phys., 2026; 20(2): 101-127

Journal of Theoretical and Applied Physics (JTAP)

https://doi.org/10.57647/jtap.2026.2002.11

Research Article

Study of Intra−Molecular C−H···O Bonded Chair Conformer of (R)−(−)−Menthyl Acetate using Combined Spectroscopic and Computational Methods

Kiran Gadivaddar, J. R. Tonannavar, Jayashree Tonannavar*

Vibrational Spectroscopy Group/Molecular Modelling Laboratory, Department of Studies In Physics, Karnatak University, Dharwad – 580003, India

***Corresponding author:** jjtonannavar@kud.ac.in

Article History:

Received:
16 August 2025

Revised:
20 September 2025

Accepted:
17 October 2025

Published Online:
05 February 2026

Published in Issue:
30 April 2026

Abstract

The intra−molecular C−H···O bond has been studied in (R)−(−)−Menthyl Acetate employing both DFT and QT-AIM methods. The B3LYP/6−311+G(d,p) level has predicted a stable chair conformation in agreement with measured IR and Raman modes. This C−H···O bonded chair conformer is also supported by a downfield shift at δ 4.68 ppm (computed δ 4.78 ppm) in the measured ^{1}H NMR spectrum and positive values of electron density and its Laplacian obtained from QT−AIM. The computed H···O distance (2.351 Å) in C–H···O bond is shorter than the sum of van der Waals radii of H and O atoms, 2.720 Å. A strong positive Cotton effect at 232 nm in the ECD spectrum corresponds to the medium UV band at 241 nm (other bands: 219 and 276 nm) and is assigned to the $n\rightarrow\pi^*$ transition. It is argued that the good agreement between computed CD band at 214 nm and its corresponding experimental band at 232 nm support proposed intra−molecular C−H···O bonded chair conformer for (R)−(−)−Menthyl Acetate. The charge delocalization in C−H···O bond is characterized by overlapping n(2)O$\rightarrow\pi^*$(C=O) natural bond orbitals with ~47 kcal/mol stabilization energy. The C−H···O bonding and its neighbor atoms are shown in terms of electron localization function and localized orbital locator as electron density distributions and their spatial locations in the interaction.

Keywords: (R)−(−)−Menthyl Acetate; NMR Spectrum; ECD Spectrum; DFT; QT−AIM analysis; ELF and LOL analyses

Cite this article: Gadivaddar, K., Tonannavar, J. R., Tonannavar, J., (2026). Study of Intra−Molecular C−H···O Bonded Chair Conformer of (R)−(−)−Menthyl Acetate using Combined Spectroscopic and Computational Methods. *J. Theor. Appl. Phys.,* 20(2), 101-127. https://doi.org/10.57647/jtap.2026.2002.11

1. Introduction

Non−covalent interactions are vital to understanding the structural, dynamic and functional characteristics of molecules, influencing their behavior in both solution and condensed phases. These interactions mainly include hydrogen bonding, van der Waals and steric interactions. Chiral molecules, being organic compounds with an asymmetric structure, are particularly susceptible to non covalent interactions, which shape their conformational

preferences and stereoselectivity. Such molecules play a central role in various fields including pharmaceuticals, where enantiomeric purity can determine drug efficacy and safety, as well as in catalysis and materials science. Understanding how non−covalent forces govern the behavior of chiral systems is essential for predicting their physical properties and designing functionally specific compounds. Among these, (R)−(−)−Menthyl acetate (shown in Figure 1) is one of the organic compound studied for its non−covalent interactions due to its distinct chiral molecular structure and the diversity of forces. This compound, commonly found in the essential oils of mint species, exhibits chiroptical properties, which provide information into its stereochemical configuration when analyzed using techniques such as UV−Vis and ECD. These properties make it an interesting subject for investigating non−covalent interactions and their role in the molecular behavior and stability of chiral compounds.

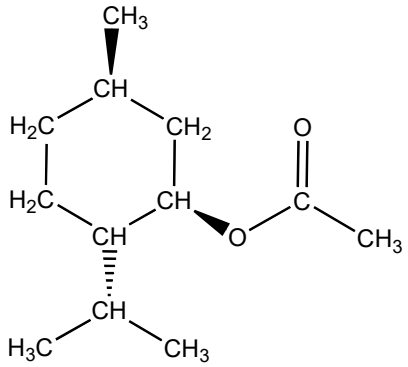

Figure 1. Schematic 2D structure of (R)−(−)−Menthyl Acetate ($C_{12}H_{22}O_2$)

(R)−(−)−Menthyl acetate (shortly RMA) is a chiral ester naturally occurring in various mint oils, particularly from *Mentha* species and is widely used for its therapeutic, aromatic and cosmetic properties [1, 2]. It is primarily obtained through the solvent extraction of *Menthapiperita* and is a derivative of menthol, formed by esterifying the hydroxyl group of menthol with an acetate group [3]. RMA is characterized by its refreshing minty aroma and cooling sensation, making it a valuable compound in the pharmaceutical industry for applications such as the treatment of throat infections, as well as possessing antifungal, antiviral and analgesic properties [4, 5]. Additionally, it finds applications in food, cosmetics and daily essential products due to its distinctive sensory attributes. The "(R)−(−)" stereochemistry notation indicates a specific spatial arrangement of substituents around the chiral center, influencing not only its biological activity but also its sensory properties. The presence of the ester functional group in RMA shows unique chemical characteristics that affect both its scent and reactivity. However, challenges such as volatility, limited aqueous solubility and instability under certain conditions suggest a deeper investigation of its molecular properties. Understanding the interactions, stability and reactivity of RMA is critical for optimizing its use in various industrial applications.

Recent reports have focused on the infrared spectra of menthyl acetate to examine its kinetics and release behavior from β−cyclodextrin complexes [1]. This work has inspired further exploration of RMA's vibrational properties. While IR studies have been conducted, comprehensive spectroscopic analyses beyond IR, including Raman, UV−Vis and ECD, have not been extensively explored for RMA. Thus, the present work aims to fill this gap by employing a combination of experimental techniques, such as IR, Raman, NMR, UV−Vis and ECD spectroscopy along with computational methods, including DFT, with Natural Bond Orbital (NBO) and Quantum Theory of Atoms in Molecules (QT−AIM) analysis. These methods will provide details of non−covalent interactions, such as hydrogen bonding, van der Waals and steric interactions, which contribute to the molecular stability and behavior of RMA.

2. Techniques and methods

2.1. Experimental

The sample RMA used in this study was procured from Sigma Aldrich Chemicals (Banglore) it is a clear colorless liquid with a boiling point above 230°C. It was directly utilized for recording IR, Raman, NMR, UV−Vis and ECD spectra.

The IR spectra were measured using a Thermo Scientific™ Nicolet™ iN10 ATR FT−IR Spectrometer with a liquid nitrogen−cooled MCT detector, covering the range of 4000−400 cm^{-1} at a spectral resolution of 4 cm^{-1}. The Raman spectra were measured using a Bruker RFS27 stand−alone FT−Raman spectrometer module equipped with an Nd:YAG laser source operating at 1064 nm. The Raman spectra were recorded in the range of 4000−50 cm^{-1} with 500 scans and a spectral resolution of 2 cm^{-1}. The detector used in this setup was a liquid nitrogen cooled Ge detector. The 400 MHz FT−NMR Spectrometer Z (JNM ECZS Series) was used to perform ^1H NMR spectral measurements in the solvent Chloroform−*d*. The signals were collected between 0 to 20 ppm with a 5 seconds relaxation delay and 32 scans at 21 °C. The UV−Vis spectra were measured on a JASCO V−670 UV−VIS−NIR double beam spectrometer equipped with a Czerny−Turner mount. The spectrum was recorded in the range of 200 to 400 nm at a speed of 1 to 200 nm per minute. The absorbance caused by the air was subtracted and baseline correction was applied. The spectrometer was equipped

with a D2 lamp as the UV−Vis radiation source and a PMT detector. The UV−Vis spectrum was measured using a $CDCl_3$ solution with a concentration of 0.1 mM. The ECD spectrum was measured using a JASCO 1500 Circular Dichroism Spectrophotometer in a wavelength range of 190 to 300 nm. The instrument featured a Xe arc lamp with nitrogen purging, a PMT detector and a double−prism monochromator. The Liquid sample was prepared in chloroform solvent and spectra were collected using quartz cuvettes with a 1 mm path length. The scans were performed at a speed of 100 nm/min.

2.2. Computational

2.2.1. *DFT calculations*

The computational investigations were conducted using an *ab initio* approach with *Gaussian 09W*, while molecular visualization and structure preparation were carried out using *Gauss View 05* [6]. Among the various Density Functional Theory, the B3LYP method was employed with the 6−311+G(d,p) basis set for geometry optimization. The optimized molecular structure of RMA, along with its atom numbering scheme, is illustrated in Figure 2. This optimized structure shows the substituent groups adopt equatorial positions in the chair conformation of the cyclohexane ring.

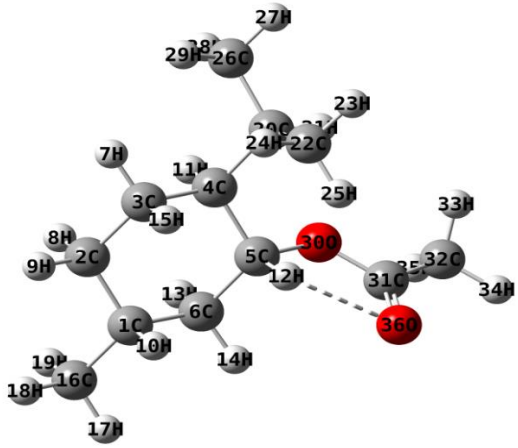

Figure 2. Optimized molecular geometrical structure of RMA with atom numbering, computed at B3LYP/6−311+G(d,p) level. The dashed line showing weak H−bond of C5−H12···O36

To explore the conformational flexibility introduced by the isopropyl and acetate groups, a Potential Energy Surface (PES) scan was performed at the ωB97X–D/6−31G level with chloroform as solvent using the Integral Equation Formalism Polarizable Continuum Model (IEFPCM) to account for solvation effects. The dihedral angles surrounding the chiral center were varied from 0 to 360° in increments of 10°. The resulting local minima were Boltzmann populated to identify the most stable conformer. The most populated conformer was further optimized at the B3LYP/6−311+G(d,p) level for cost–effectiveness and employed in subsequent simulations. Harmonic vibrational frequency calculations were carried out at the same level and appropriately scaled using a scale factor to achieve better agreement with the experimental IR frequencies [7]. Potential Energy Distributions (PED) were derived using the *VEDA 4.0* package to aid in the assignment of vibrational modes [8].

Further electronic structure analyses included NBO, UV−Vis and ECD studies, all carried out at the B3LYP/6−311++G(d,p) level [9−14]. QT−AIM analysis was employed to examine the topological characteristics of electron density, including the Laplacian and energy descriptors at bond critical points (BCPs) and ring critical points (RCPs) [15]. Additionally, NCI analysis was conducted using *Multiwfn 3.8* and *VMD* software, enabling visualization of van der Waals and steric interactions through reduced density gradient isosurfaces [16, 17]. Complementary analyses such as Electron Localization Function (ELF), Localized Orbital Locator (LOL) and Interaction Region Indicator (IRI) were performed to further explore localized electron distributions, bonding nature and interaction regions within the molecule [18−20].

3. Results and discussion

3.1. Optimized molecular geometry analysis

The RMA molecule contains three substituents, methyl, acetate and isopropyl groups attached at the ortho, meta and para positions respectively, in relation to the chair conformation of the cyclohexane ring. To investigate the conformational behavior, a scan was carried out on the mod−redundant dihedral coordinate C5*−C4*−C20−C26 (where * denotes the chiral center), rotating the C4*−C20 bond in 36 steps with 10° increments. This process produced multiple conformers. Among these conformers, one conformer stood out as the most energetically favorable, with a Boltzmann population of 76.83%, as shown in Table 1. This conformer was subject to a further PES scan around the dihedral angle C5*−O30−C31−O36, which shows two local minima: conformers g1 and g2, with respective energies of −620.674297261 and −620.66614216 Hartree, as illustrated in Figure S1. The population analysis indicated that conformer g1 is the lowest with 99.98% population, while g2 contributes only 0.02% (Table 2). Conformer g1 was then selected for geometry optimization and optimized at B3LYP/6−311+G(d,p) level. The optimized structure is shown in Figure 2 and its key geometrical parameters are listed in Table 3.

Table 1. Boltzmann population for PES scan of dihedral angle C5−C4−C20−C26 computed at ωB97X–D/6–31G level of RMA

Sl. No.	Conformers	Energy (Hartree)	ΔG (Hartree)	ΔG (kcal/mol)	Population%
1	g1'	−620.878	0	0	76.83
2	g2'	−620.876	0.0012	0.76195	21.39
3	g3'	−620.873	0.0042	2.65414	0.89
4	g4'	−620.873	0.0042	2.66254	0.88

Table 2. Boltzmann population for PES scan of dihedral angle C5−O30−C31−O36 computed at ωB97X–D/6–31G level of RMA

Sl No.	Conformers	Energy (Hartree)	ΔG (Hartree)	ΔG (kcal/mol)	Population%
1	g1	−620.674	0	0	99.98
2	g2	−620.666	0.0082	5.11741	0.02

Table 3. Optimized geometrical parameters of conformer g1 of RMA computed at B3LYP/6−311+G(d,p)

Bond length (Å)					
Parameters	Values	Parameters	Values	Parameters	Values
C1−H10	1.100	C22−H23	1.097	C2−C3	1.546
C2−H8	1.099	C22−H24	1.096	C3−C4	1.550
C2−H9	1.098	C22−H25	1.094	C4−C5	1.538
C3−H7	1.095	C26−H27	1.096	C4−C20	1.558
C3−H15	1.098	C26−H28	1.097	C5−C6	1.532
C4−H11	1.100	C26−H29	1.096	C20−C22	1.547
C5−H12	1.092	C32−H33	1.095	C20−C26	1.546
C6−H13	1.098	C32−H34	1.090	C31−C32	1.514
C6−H14	1.097	C32−H35	1.094	<C−C>	1.542
C16−H17	1.096	<C−H>	1.096	C5−O30	1.496
C16−H18	1.096	C1−C2	1.546	O30−C31	1.385
C16−H19	1.097	C1−C6	1.546	C31−O36	1.228
C20−H21	1.098	C1−C16	1.542		
Bond angle (°)					
C2−C1−H10	108.099	C20−C26−H27	110.078	H23−C22−H24	107.704
C6−C1−H10	108.223	C20−C26−H28	111.06	H23−C22−H25	107.909
C1−C2−H8	108.618	C20−C26−H29	111.001	H24−C22−H25	109.412
C1−C2−H9	109.634	C31−C32−H33	109.320	H27−C26−H28	108.272
C3−C2−H8	109.241	C31−C32−H34	109.557	H27−C26−H29	107.857
C3−C2−H9	110.010	C31−C32−H35	109.557	H28−C26−H29	108.468
C2−C3−H7	109.641	<C−C−H>	109.685	H33−C32−H34	110.118
C2−C3−H15	109.138	H10−C1−C16	108.773	H33−C32−H35	107.652
C4−C3−H7	109.719	H11−C4−C20	106.963	H34−C32−H35	110.604
C4−C3−H15	109.507	H21−C20−C22	108.032	<H−C−H>	108.603
C3−C4−H11	107.909	H21−C20−C26	107.685	C2−C1−C6	109.535
C5−C4−H11	106.798	<H−C−C>	107.863	C1−C2−C3	111.606
C4−C5−H12	111.145	C4−C5−O30	108.726	C2−C3−C4	111.154
C6−C5−H12	111.030	C6−C5−O30	106.452	C3−C4−C5	107.694
C1−C6−H13	109.575	<C−C−O>	107.589	C4−C5−C6	111.918
C1−C6−H14	110.273	H12−C5−O30	107.324	C1−C6−C5	110.966

Table 3. Optimized geometrical parameters of conformer g1 of RMA computed at B3LYP/6−311+G(d,p) (Continued)

Parameters	Values	Parameters	Values	Parameters	Values
C5−C6−H13	108.528	C5−O30−C31	117.231	<C−C−C>	110.479
C5−C6−H14	109.381	O30−C31−C32	109.043	C6−C1−C16	110.847
C1−C16−H17	110.943	O30−C31−O36	124.090	C2−C1−C16	111.269
C1−C16−H18	110.741	H8−C2−H9	107.635	C3−C4−C20	114.439
C1−C16−H19	110.077	H7−C3−H15	107.609	C5−C4−C20	112.679
C4−C20−H21	105.554	H13−C6−H14	108.051	C4−C20−C22	113.608
C20−C22−H23	109.581	H17−C16−H18	108.361	C4−C20−C26	111.088
C20−C22−H24	110.983	H17−C16−H19	108.321	C22−C20−C26	110.539
C20−C22−H25	111.14	H18−C16−H19	108.316	<C−C−C>	111.334
		Dihedral angle (°)			
C6−C1−C2−C3	−54.961	H9−C2−C3−H15	58.766	O30−C5−C6−C1	−177.95
C6−C1−C2−H8	65.533	C2−C3−C4−C5	−58.004	O30−C5−C6−H13	−57.492
C6−C1−C2−H9	−177.11	C2−C3−C4−H11	56.949	O30−C5−C6−H14	60.175
H10−C1−C2−C3	62.752	C2−C3−C4−C20	175.872	C4−C5−O30−C31	118.159
H10−C1−C2−H8	−176.75	H7−C3−C4−C5	−179.44	C6−C5−O30−C31	−121.11
H10−C1−C2−H9	−59.392	H7−C3−C4−H11	−64.487	H12−C5−O30−C31	−2.154
C16−C1−C2−C3	−177.87	H7−C3−C4−C20	54.437	C4−C20−C22−H23	−178.74
C16−C1−C2−H8	−57.377	H15−C3−C4−C5	62.661	C4−C20−C22−H24	−59.919
C16−C1−C2−H9	59.984	H15−C3−C4−H11	177.614	C4−C20−C22−H25	62.083
C2−C1−C6−C5	55.318	H15−C3−C4−C20	−63.463	H21−C20−C22−H23	64.511
C2−C1−C6−H13	−64.512	C3−C4−C5−C6	59.238	H21−C20−C22−H24	−176.67
C2−C1−C6−H14	176.677	C3−C4−C5−H12	−65.538	H21−C20−C22−H25	−54.663
H10−C1−C6−C5	−62.318	C3−C4−C5−O30	176.543	C26−C20−C22−H23	−53.077
H10−C1−C6−H13	177.853	H11−C4−C5−C6	−56.449	C26−C20−C22−H24	65.747
H10−C1−C6−H14	59.041	H11−C4−C5−H12	178.775	C26−C20−C22−H25	−172.25
C16−C1−C6−C5	178.479	H11−C4−C5−O30	60.856	C4−C20−C26−H27	−172.02
C16−C1−C6−H13	58.649	C20−C4−C5−C6	−173.61	C4−C20−C26−H28	−52.12
C16−C1−C6−H14	−60.163	C20−C4−C5−H12	61.618	C4−C20−C26−H29	68.639
C2−C1−C16−H17	−179.13	C20−C4−C5−O30	−56.302	H21−C20−C26−H27	−56.893
C2−C1−C16−H18	−58.758	C3−C4−C20−H21	−179.69	H21−C20−C26−H28	63.006
C2−C1−C16−H19	60.99	C3−C4−C20−C22	62.13	H21−C20−C26−H29	−176.24
C6−C1−C16−H17	58.718	C3−C4−C20−C26	−63.244	C22−C20−C26−H27	60.909
C6−C1−C16−H18	179.088	C5−C4−C20−H21	56.828	C22−C20−C26−H28	−179.19
C6−C1−C16−H19	−61.164	C5−C4−C20−C22	−61.356	C22−C20−C26−H29	−58.434
H10−C1−C16−H17	−60.154	C5−C4−C20−C26	173.271	C5−O30−C31−C32	176.883
H10−C1−C16−H18	60.216	H11−C4−C20−H21	−60.231	C5−O30−C31−O36	−3.732
H10−C1−C16−H19	179.964	H11−C4−C20−C22	−178.42	O30−C31−C32−H33	62.117
C1−C2−C3−C4	57.721	H11−C4−C20−C26	56.211	O30−C31−C32−H34	−177.13
C1−C2−C3−H7	179.203	C4−C5−C6−C1	−59.283	O30−C31−C32−H35	−55.63
C1−C2−C3−H15	−63.162	C4−C5−C6−H13	61.17	O36−C31−C32−H33	−117.25
H8−C2−C3−C4	−62.407	C4−C5−C6−H14	178.837	O36−C31−C32−H34	3.506
H8−C2−C3−H7	59.075	H12−C5−C6−C1	65.557	O36−C31−C32−H35	125.007
H8−C2−C3−H15	176.71	H12−C5−C6−H13	−173.99	H12−C5−C6−H14	−56.324
H9−C2−C3−C4	179.649	H9−C2−C3−H7	−58.869		

Since no direct experimental data for the geometry of RMA is available, the optimized bond lengths, bond angles and dihedral angles of g1 were compared with electron diffraction (ED) data of structurally related compounds: (−)−Menthol (EDM) and (+)−Isomenthol (EDI) [21] (see Table 4). The analysis shows that the average C–C bond lengths in RMA is 1.545 Å, which is slightly elongated compared to both (−)−Menthol (1.534 Å) and (+)−Isomenthol (1.538 Å), with deviations of 0.72 and 0.46%, respectively. The C5–O30 bond (the ester linkage) in RMA is significantly longer (1.496 Å) than the corresponding C–O bond in (−)−Menthol (1.408 Å) and (+)−Isomenthol (1.427 Å), showing deviations of 6.24 and 4.83%, respectively. This elongation is attributed to the influence of the acetate group, which induces greater electron withdrawal and bond stretching. Similarly, slight variations are observed in ring bond angles and other structural features. For instance, the average C–C–C bond angle within the cyclohexane ring in RMA (⟨C–C–Cring⟩ = 110.668°) is lower than in (−)−Menthol (112.200°) and (+)−Isomenthol (112.600°), with deviations of 1.37 and 1.72%, respectively. The dihedral angle C3–C4*–C20–C22 in RMA is 62.13°, which deviates by 9.00° from (−)−Menthol and 1.38° from (+)−Isomenthol.

Table 4. Comparison of optimized geometrical parameters of conformer g1 of RMA computed at B3LYP/6−311+G(d,p) to (−)−Menthol (EDM) and (+)−isomenthol (EDI) [21]

Parameters	RMA (g1)	(−)−Menthol	(+)−isomenthol	Deviation %	
		EDM	EDI	EDM−g1	EDI−g1
Bond lengths (Å)					
C1−C2	1.546	1.533	1.540	0.83	0.38
C2−C3	1.546	1.531	1.535	1.01	0.74
C3−C4	1.550	1.538	1.541	0.75	0.56
C4−C5	1.538	1.533	1.536	0.31	0.12
C5−C6	1.532	1.530	1.534	0.16	0.10
C6−C1	1.546	1.533	1.540	0.87	0.42
C1−C16	1.542	1.528	1.536	0.94	0.41
Bond lengths (Å)					
C4−C20	1.558	1.550	1.552	0.48	0.35
C20−C22	1.547	1.533	1.535	0.93	0.79
C20−C26	1.546	1.532	1.535	0.90	0.70
<C−C>	1.545	1.534	1.538	0.72	0.46
C5−O30	1.496	1.408	1.427	6.24	4.83
Bond angle (°)					
C1−C2−C3	111.606	112.900	113.800	1.15	1.93
C2−C3−C4	111.154	113.200	113.200	1.81	1.81
C3−C4−C5	107.694	110.300	110.500	2.36	2.54
C4−C5−C6	111.918	112.500	112.500	0.52	0.52
C5−C6−C1	110.966	113.900	115.000	2.58	3.51
C2−C1−C6	109.535	110.400	110.400	0.78	0.78
<C−C−C_{ring}>	110.668	112.200	112.600	1.37	1.72
C2−C1−C16	111.269	111.200	111.400	0.06	0.12
C6−C1−C16	110.847	110.900	111.600	0.05	0.67
C3−C4−C20	114.439	113.600	113.400	0.74	0.92
C5−C4−C20	112.679	112.000	111.600	0.61	0.97
C4−C20−C22	113.608	113.200	113.000	0.36	0.54
C4−C20−C26	111.088	110.700	110.400	0.35	0.62
C22−C20−C26	110.539	109.600	109.300	0.86	1.13
<C−C−C>	111.334	111.877	111.877	0.49	0.49
C4−C5−O30	108.726	108.400	107.600	0.30	1.05
C6−C5−O30	106.452	111.600	110.500	4.61	3.66
<C−C−O>	107.589	110.000	109.050	2.19	1.34
<C−C−H>	109.550	109.200	108.900	0.32	0.60
Dihedral angle (°)					
C3−C4−C20−C22	62.130	57.000	−63.000	9.00	1.38

Table 5. Comparison of the computed optimized geometry properties of the C–H···O hydrogen bonding of RMA at B3LYP/6−311+G(d,p) level with typical characteristics of weak hydrogen bonds as described by Desiraju et. al. [22]

Properties	Typical Range*	Computed C5−H12···O36
X–H bond length (Å)	1.083	1.0919
Bond energy (kcal/mol)	< 4.0 kcal/mol	E_{int} = –6.52 & E_{BE} = –3.16
H···A vs. X···H bond lengths (Å)	H···A >> X···H	H12···O36 = 2.351 > C5···H12 = 1.0919
X–H bond lengthening (Å)	< 0.1	0.0089
X···A (Å)	3.0 – 4.0	C5···O36 = 3.4429
H···A (Å)	2.0 – 3.0	H12···O36 = 2.351
Bond shorter than van der Waals distance	30–80% of van der Waals (H···O = 2.72 Å)	H12···O36 = 2.351 Å → 13.57% shorter
∟X–H···A (º)	90 – 180	C5–H12···O36 = 98.36

Note : X = Donor, H= Hydrogen and A= Acceptor. X–H···A = Hydrogen bond.
* = Reported values by Desiraju et. al. [22]

The geometrical parameters for C5–H12···O36 H−bond in RMA shows clear evidence of a weak non−covalent interaction according to reported values as shown in Table 5 [22]. The calculated C5–H12 bond length (1.091 Å) is slightly longer than the typical value (1.083 Å), which is a common sign of hydrogen bond (H–bond) involvement. The interaction energy values (E_{int} = –6.52 and –3.16 kcal/mol) are stronger than what is usually expected for weak H–bonds, suggesting a more pronounced interaction in this case. The H12···O36 distance (2.351 Å) fits well within the normal range of 2.0 to 3.0 Å and is about 13.6% shorter than the van der Waals limit, indicating a significant attraction. Other geometric parameters, such as the C5···O30 distance (3.442 Å) and the small C5–H12 bond elongation (0.008 Å), also fall within expected ranges and support the presence of a weak H−bond. The bond angle (C5–H12···O36 = 98.36°) lies within the typical range of 90°–180°, confirming its directional nature; although more acute than classical strong hydrogen bonds, it still provides measurable stabilization. To quantify this, the H–bonded conformer (g1) and non–H–bonded conformer (g2) were optimized at the ωB97X–D/6−31G (IEFPCM, chloroform) level (Figure S1), where g2 was found ~5 kcal mol^{-1} higher in free energy, demonstrating that even the bent interaction contributes significantly to stability.

The acute geometry can be attributed to steric restrictions from the isopropyl and acetate groups, which prevent linear alignment, while favorable $n(O)\rightarrow\sigma^*(C–H)$ orbital overlap provides stabilization. This interaction was further explored by NBO and QT–AIM analyses. Overall, the computed geometry agrees with known features of weak hydrogen bonding [22], confirming the presence of a structurally relevant C–H···O interaction in RMA.

3.2. NMR spectral analysis

The proton NMR spectrum of RMA in $CDCl_3$ (residual solvent peak at δ 7.26 ppm [23]) exhibits well−resolved peaks (see Figure 3) that provide evidence for weak intra−molecular C−H···O bonding within the molecule. The comparison and assignment of the experimental and calculated ^{1}H NMR chemical shifts at the B3LYP/6−311+G(d,p) level, using the gauge−independent atomic orbitals (GIAO) method, are presented in Table 6. The methine proton adjacent to the ester oxygen resonates at δ 4.68 ppm, showing a downfield shift compared to typical aliphatic O–CH environments (~3.90 ppm). The H−bonded conformer reproduces this shift accurately (δ_B = 4.78 ppm), while the non−H−bonded conformer gives δ_{NB} = 3.75 ppm, which matches the reported typical CH resonance (δ ≈ 3.90 ppm). This clear distinction demonstrates that the experimentally observed deshielding arises specifically from C5–H12···O36 hydrogen bonding. The distance between this methine proton and the carbonyl oxygen (2.350 Å) is shorter than the combined van der Waals radii (2.720 Å), indicating a moderate intra−molecular interaction contributing to the observed deshielding [22]. This downfield shift arises from a decrease in electron density around the methine proton at C5–H12···O36 bond [22, 23]. It indicates deshielding influenced by the anisotropic effect of the adjacent carbonyl group and nearby C–H···O intra−molecular interaction. This shift clearly indicates that the H–bond does not induce shielding in this geometry. Instead, the spatial positioning within the deshielding zone of the carbonyl's anisotropic field leads to a downfield shift, confirming the electronic influence of both the carbonyl group and the C–H···O H–bond. The methyl protons of the acetate group appear at δ 2.03 ppm, close to the computed values for both H−bonded (δ_B = 1.84 ppm) and non−H−bonded (δ_{NB} = 1.90 ppm) conformers. These small variations show that the acetate methyl group is only weakly perturbed by hydrogen bonding (see Table 6 and Figure S2) [24–26]. The multiplet centered at δ 1.87 ppm corresponds to the methylene and methine protons within the cyclohexane ring and isopropyl group, as shown in Figure 3(a).

Table 6. Comparison of experimental ^{1}H NMR chemical shifts (δ) for RMA in $CDCl_3$ with computed values for the RMA monomer (H−bonded (δ_B) and non−H−bonded (δ_{NB}))at the B3LYP/6−311+G(d,p) level based on GIAO method

Chemical Shifts, δ, (ppm)	Frequency* (Hz)	Reporteda,b δ, (ppm)	Computed RMA		Assignments
			δ_B(ppm)	δ_{NB} (ppm)	
7.51	2923.7	7.26	–	–	$CDCl_3$
4.68	1872	3.90	4.78	3.75	CH(Ring at O)
2.17	867.7	2.01	1.30	2.19	CH(near isopropyl)
2.03	812.4	1.90	1.84	1.90	CH_3(at acetate)
1.97	789.3	1.52	1.57	1.56	CH_2(ring)
1.87	745.8	1.82	1.96	1.29	CH(ring near isopropyl)
1.68	672.3	1.61	1.39	1.30	CH(near methyl)
1.48	590.9	1.27	0.80	0.84	CH_2(ring)
1.36	544.1	1.76−1.51	1.34	1.38	CH_2(ring)
0.98	391	1.27	0.97	0.90	CH_2(ring)
0.89	354.9	1.06	0.86	0.88	CH_3(methyl)
0.77	309.3	1.01	0.65	0.65	CH_3(isopropyl)

Note: * = Resonance frequencies of protons that are higher than the resonance frequency of TMS.a = [25],b = [22]

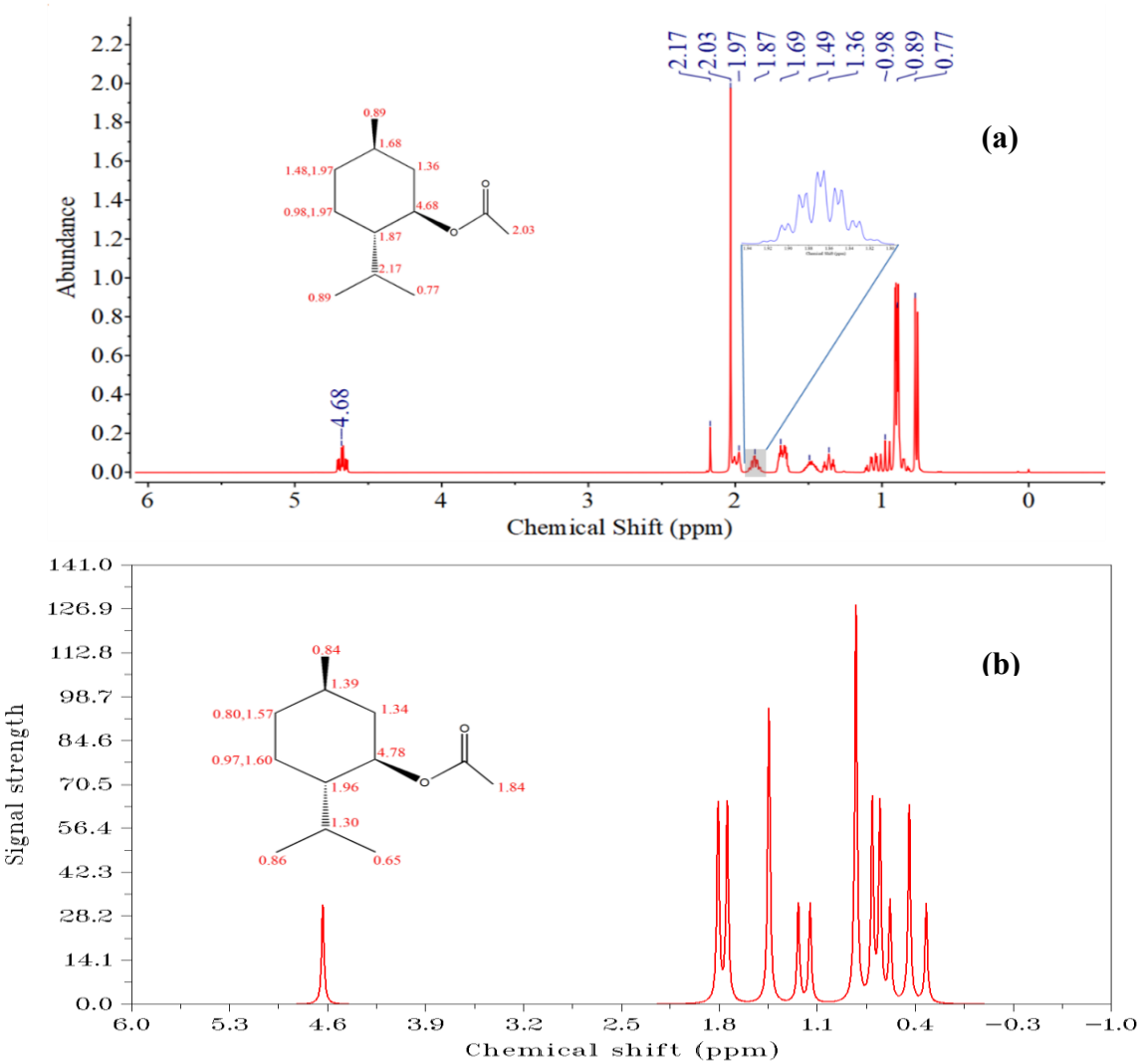

Figure 3. (a) Experimental ^{1}H NMR spectrum of RMA recorded in $CDCl_3$, with assigned chemical shifts labeled on the molecular structure. The inset for a magnified view of the region around δ 1.87 ppm for clearer visualization of the multiplet. (b) Simulated ^{1}H NMR spectrum of RMA (g1 conformer) computed at B3LYP/6−311++G(d,p) level based on GIAO method

10.57647/jtap.2026.2002.11

The complexity and breadth of this signal indicate multiple environments for these protons, influenced by the rigid ring structure and the presence of bulky substituents. Steric interactions within the ring can lead to conformational constraints, causing variations in the local magnetic environment and resulting in the observed multiplet structure [24, 27]. For the methine proton near the isopropyl substituent, the experimental δ 1.87–2.01 ppm correlates best with the H−bonded conformer value (δ_B = 1.96 ppm), while the non−H−bonded conformer (δ_{NB} = 1.29 ppm) significantly underestimates the shift. This again confirms that hydrogen bonding induces localized deshielding effects. In contrast, other methylene and methyl groups in the ring region show minimal differences (<0.2 ppm) between δ_B and δ_{NB}, reflecting their distance from the H−bonding site. The Signals at δ 1.68, 1.48 and 1.36 ppm are attributed to ring methylene groups in shielded environments, while the shielded methyl resonances at δ 0.98–0.77 ppm correspond to methyl groups in equatorial orientations of the cyclohexane chair and isopropyl branch. The H−bonded conformer consistently shows good agreement with experiment in regions of deshielding, whereas the non−H−bonded conformer reproduces the typical literature values for unperturbed CH environments.

The ^{1}H NMR spectrum of RMA in $CDCl_3$ thus strongly supports a chair conformation of the cyclohexane ring, stabilized by both bulky substituents and intra−molecular C–H···O interactions. The downfield resonance at δ 4.68 ppm, in particular, serves as a distinct NMR signature of intra−molecular hydrogen bonding, complementing the spectroscopic and computational evidence for non−covalent interactions in RMA. Multiple non−equivalent chemical shifts observed for CH and CH_2 protons between δ 1.97 and 0.98 ppm reflect distinct axial and equatorial environments, indicating that the ring is conformationally locked. This rigidity arises from steric effects of the isopropyl and ester substituents, which constrain the ring geometry. The equatorial positioning of the proton adjacent to the ester group further supports the chair model, as steric hindrance disfavors an axial orientation. Additionally, the shielded methyl resonances at δ 0.89 and 0.77 ppm are consistent with equatorial positions, typical of the chair form where such groups experience less deshielding. The close agreement between experimental and computed shifts confirms the stable chair conformation of RMA, stabilized jointly by steric and C−H···O interactions.

3.3. Vibrational analysis

The observed IR and Raman spectra are shown in Figure 4. Comparative analyses between the computed and observed data of IR and Raman spectra are presented in Figure 5 and Figure 6, while detailed assignments are elucidated in Table 7.

The statistical analysis (MAE, RMSD and deviation%) of vibrational frequencies for the observed IR/Raman and the computed C–H···O bonded and non−bonded conformers is presented in Table S1 and Table S2.

In the monomeric structure of RMA, four CH_3 groups collectively exhibit asymmetric C–H stretching at 2954 cm^{-1} (IR) and 2937 cm^{-1} (Raman), closely corresponding to the computed values of 2954 and 2935 cm^{-1}, respectively.

The CH symmetric stretching modes of both CH_3 and CH_2 groups were identified at 2921 cm^{-1} (IR), closely aligning with the computed value of 2922 cm^{-1}. The IR and Raman peaks observed at 2870 and 2871 cm^{-1}, attributed to symmetric CH stretching.

The 3019 and 3024 cm^{-1} bands from IR and Raman depicted to CH vibrations in methyl group and is deviated by 0.20 and 0.36 % with excellent agreement from computed value 3013 cm^{-1}.

The distinctive CH deformations within the methyl groups were at 1454 and 1369 cm^{-1} (IR), along with 1461 and 1377 cm^{-1} (Raman), respectively. The predicted values closely aligned at 1454, 1370 (IR) and 1463, 1380 cm^{-1} (Raman), signifying specific structural correlations. Gouyong Zhu et. al. experimental IR analysis of menthyl acetate reported absorption bands at 2922 and 2870 cm^{-1} for C–H stretching, 1736 cm^{-1} for C=O stretching, 1451 and 1370 cm^{-1} for C–H deformation and 1242 cm^{-1} for C–O stretching.

These features closely align with the observed RMA spectrum, which showed corresponding peaks at 2921, 2870, 1734, 1454, 1369 and 1237 cm^{-1}, respectively, confirming the reliability of the spectral assignment and its consistency with structural modifications in RMA [28].

The observed band at 1734 (IR) and 1735 cm^{-1} (Raman), it is predicted at 1728 cm^{-1} corresponds to C=O stretching vibrational mode. The weak C–H···O interaction frequencies are not observed in the IR spectrum, suggesting that H–bonding in RMA slightly alters the electron density around the carbonyl group without causing significant red or blue shifts.

The structural derivation of RMA from menthol, by substituting the OH group with an acetate group, significantly impacts its vibrational characteristics. A comparative analysis with the vibrational data reported by Toru Egawa et. al. shows key vibrational shifts that underscore this modification [21].

The C=O stretching appears at 1734 cm^{-1}, CH_3 deformation at 1369 cm^{-1}, C–O stretching at 1237 cm^{-1}, O–C=O deformation at 651 cm^{-1} and C=O wagging at 609 cm^{-1} in experimental IR data for presence of acetate

substituent in RMA. Corresponding computed values were found at 1728, 1370, 1233, 632 and 594 cm^{-1}, respectively. Similarly, the IR bands at 2921, 2870, 1454, 1369, 904 and 842 cm^{-1}, along with the Raman bands at 2870, 1460, 1375, 905, 576, 334, 315 and 291 cm^{-1}, confirms the presence of the cyclohexane ring in the chair form of RMA, as summarized in Table 7, which is further supported by the distinct non−equivalent proton environments observed in the ^1H NMR spectrum.

The low–frequency vibrational analysis (<400 cm^{-1}) highlights Raman−active torsional and librational modes as signatures of intra−molecular stabilization in RMA. An experimental Raman band at 72 cm^{-1} is reproduced at 79 cm^{-1} in the H−bonded conformer, corresponding to coupled COCC and HCCO torsions, whereas the non−H−bonded conformer predicts this mode at 122 cm^{-1} and also exhibits a soft mode near 70 cm^{-1} due to mode mixing in the absence of C–H···O interaction (Table S1). The deviation from experiment is only 9.17% for the H−bonded conformer versus 54.43% for the non−bonded conformer, confirming the stabilizing role of the H−bond. Weaker Raman bands at 315, 291, 262, 228 and 178 cm^{-1} are well reproduced (computed at 298, 279, 274, 227 and 192 cm^{-1}) and correspond to HCCC, CCCC torsional and CCC bending modes.

The H−bonded conformer differs from the non−H−bonded one by 3.15% and average deviations from experimental IR and Raman frequencies are 1.37 and 1.53% for H−bonded and 2.18 and 5.16% for non−H−bonded, respectively (Table S2).

These results indicate that low−frequency torsions reliably reflect restricted flexibility and conformational stabilization induced by intra−molecular C–H···O interactions.

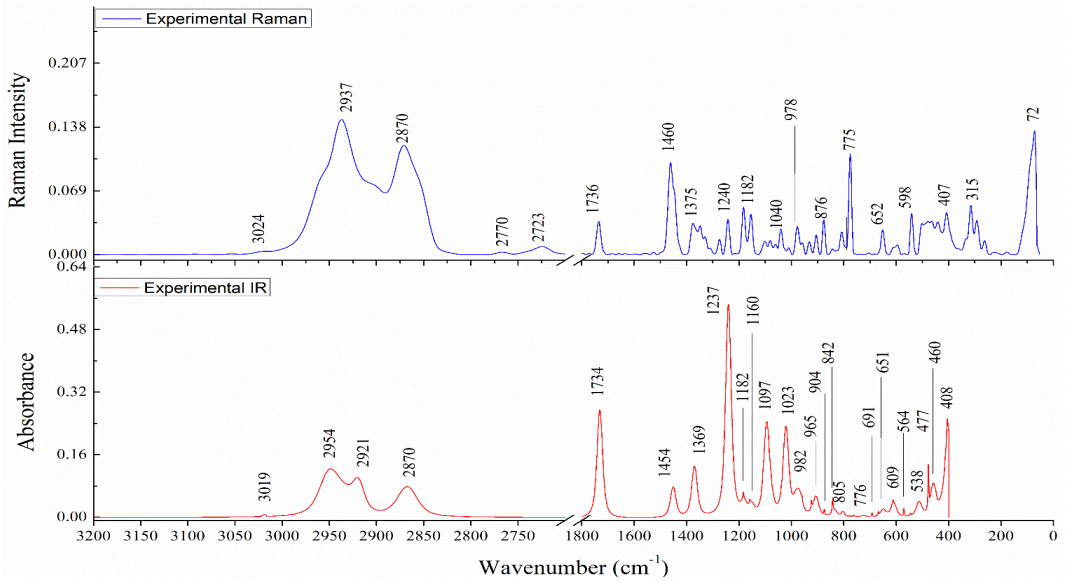

Figure 4. Comparison of experimental IR and Raman spectra of RMA. Break in the Wavenumber (2700 to 1800 cm^{-1}) for neat observation

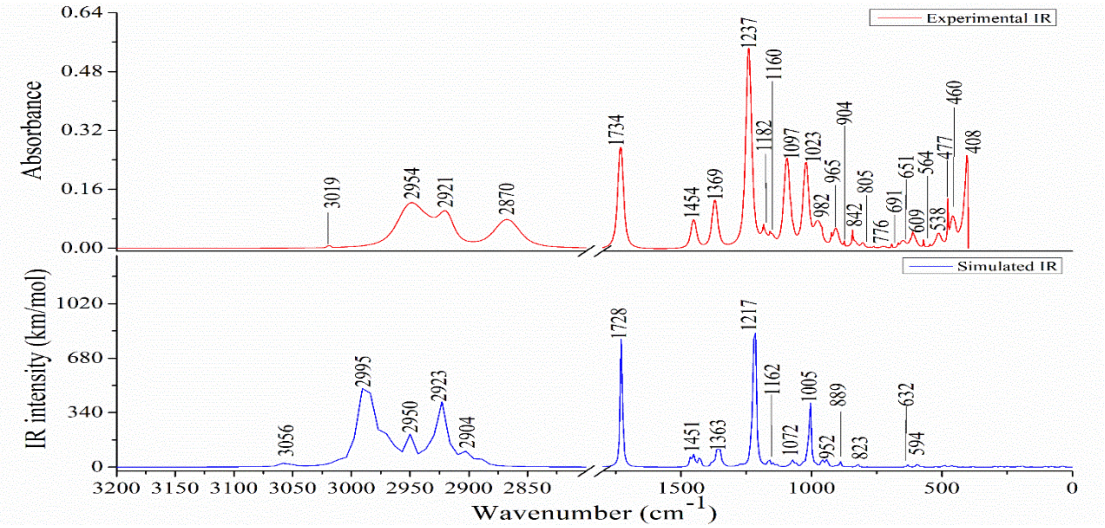

Figure 5. Comparison of experimental and simulated IR spectra of RMA, computed at B3LYP/6−311+G(d,p) level. Break in the Wavenumber (2700 to 1800 cm^{-1}) for neat observation

10.57647/jtap.2026.2002.11

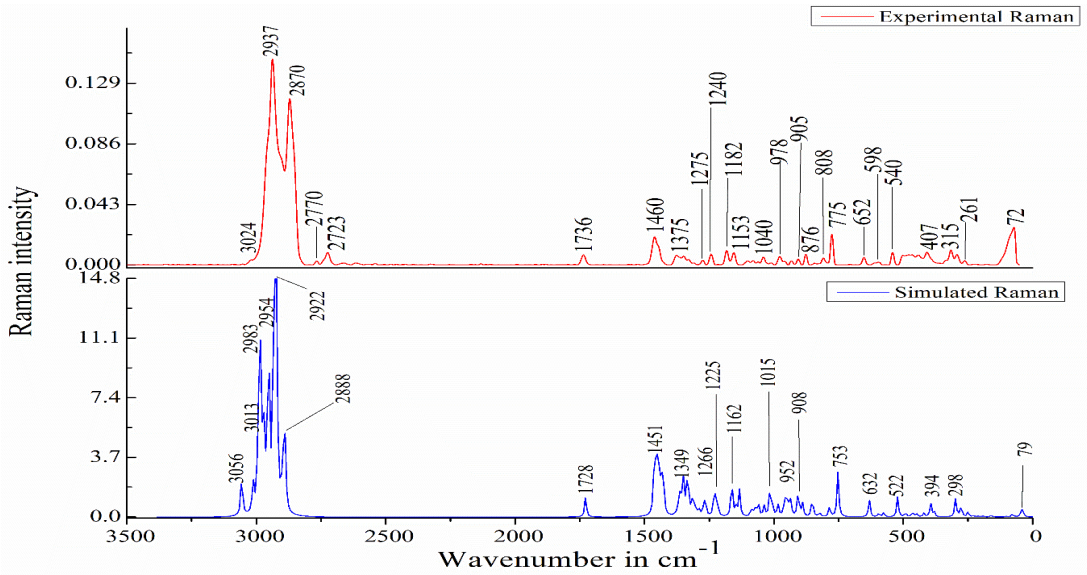

Figure 6. Comparison of experimental and simulated Raman spectra of RMA, computed at the B3LYP/6−311+G(d,p) level

Table 7. Comparison between Experimental and Computed Vibrational Frequencies of IR and Raman spectra for RMA with assignments and PED %

Frequencies (cm^{-1})								
Computed						Experimental		Assignments [PED%]
Conformer (g1)				Conformer (g2)				
υ_{un}	υ_{sc}*	I_{IR}	I_{Raman}	υ_{un}	υ_{sc}*	IR	Raman	
3154	3056	8.33	290.12	3140	3042	–	–	υ_s CH on CH_3^{IV}[90]
3110	3013	5.91	208.05	3096	2999	3019w	3024w	υ_{as} CH on CH_3^{IV}[100]
3091	2995	30.24	191.30	3082	2986	–	–	υ_{as} CH on CH_3^{I} [90]
3086	2989	87.55	324.70	3077	2981	–	–	υ_{as} CH on CH_3^{I}& CH_3^{II}[89]
3083	2987	32.06	359.62	3074	2978	–	–	υ_{as} CH on CH_3^{III}[98]
3082	2986	43.40	339.48	3073	2978	–	–	υ_{as} CH on CH_3^{I}& CH_3^{II}[85]
3081	2985	24.42	321.66	3073	2977	–	–	υ_{as} CH on CH_3^{II}[86]
3079	2983	2.42	74.59	3070	2975	–	–	υ_{as} CH on CH_3^{I}& CH_3^{II}[90]
3075	2979	41.17	347.60	3067	2972	–	–	υ_{as} CH on CH_3^{III}[91]
3065	2969	26.25	494.47	3060	2965	–	–	υ_{as} CH on CH_2[70]
3062	2967	30.07	75.79	3051	2956	–	–	υ_{as} CH on CH_2[76]
3050	2954	2.93	708.37	3045	2950	2954m	–	υ_{as} CH on CH_3^{IV}[90]
3045	2950	48.32	539.88	3038	2944	–	–	υ_{as} CH on CH_2[82]
3029	2935	9.42	351.51	3032	2938	–	2937vs	υ_s CH on isopropyl[92]
3026	2932	25.37	1297.86	3012	2918	–	–	υ_s CH on CH_3^{I}[76]+υ_{as} CH of CH_2 on ring[19]
3018	2924	30.24	335.94	3011	2917	–	–	υ_s CH on CH_3^{II}[16]+υ_s CH of CH_3^{III}[78]
3017	2923	61.24	579.08	3008	2914	–	–	υ_s CH of CH_3^{III}& CH_2 on ring[86]
3016	2922	17.24	653.52	3004	2910	2921m	–	υ_s CH of CH_3^{III}& CH_2 on ring[81]
3010	2916	11.29	45.30	3002	2909	–	–	υ_s CH of CH_3^{III}& CH_2 on ring[85]
2998	2904	24.48	123.71	2997	2903	–	–	υ_s CH of CH_2 on ring[77]
2987	2894	6.91	450.51	2996	2903	–	–	υ_s CH on ring[89]
2982	2888	8.01	388.35	2986	2892	2870m	2870vs	υ_{as} CH on ring[86]
1784	1728	261.05	92.08	1703	1649	1734s	1736w	υ C=O [87]
1512	1465	9.40	45.81	1511	1464	–	–	β CH_3^{I}& CH_3^{II}[79]
1510	1463	6.72	161.98	1511	1464	–	1460m	βs CH_3^{II}[69]
1502	1455	2.90	196.93	1503	1456	–	–	βs CH_2 and CH_3^{III} on ring[68]
1500	1454	6.65	174.97	1501	1454	1454m	–	βs CH_2 on ring[33]+βs CH_2 on ring[25]
1499	1453	12.09	29.89	1500	1453	–	–	βs CH_3^{I}& CH_3^{II} and βs CH_2[77]+ βs CH_3^{III} on ring[77]
1497	1451	2.38	13.77	1498	1451	–	–	βs CH_3^{I}& CH_3^{II} and βs CH_2[64]+ βs CH_3 on ring [64]
1493	1446	3.34	42.04	1493	1447	–	–	βs CH_2 on ring[78]
1489	1443	1.99	189.90	1491	1444	–	–	βs CH_3^{I}& CH_3^{II}[76]
1485	1439	0.26	70.45	1488	1442	–	–	βd CH_2 on ring[74]
1478	1432	9.85	151.12	1484	1438	–	–	βd CH_3^{IV}[90]

Table 7. Comparison between Experimental and Computed Vibrational frequencies of IR and Raman spectra for RMA with assignments and PED % (Continued)

Frequencies (cm^{-1})								
Computed						Experimental		Assignments [PED%]
Conformer (g1)				Conformer (g2)				
υ_{un}	υ_{sc}*	I_{IR}	I_{Raman}	υ_{un}	υ_{sc}*	IR	Raman	
1472	1426	13.82	140.14	1473	1427	–	–	βd CH_3^{IV}[86]
1425	1380	10.30	10.53	1418	1374	–	1375w	ϒw CH_3^{I} and CH_3^{II} [62]
1414	1370	4.77	40.86	1410	1366	1369m	–	βd CH_3^{III}[62]
1406	1363	12.47	56.36	1405	1361	–	–	ϒw CH on ring[55]
1405	1361	5.92	57.59	1399	1356	–	–	τ HCCC [12]
1403	1359	23.23	38.54	1397	1353	–	–	ϒw HCC[56]
1394	1351	24.34	111.33	1394	1351	–	–	ϒw HCC[56]
1392	1349	3.06	120.60	1386	1343	–	1346w	βr CH[45]
1384	1341	4.71	16.41	1373	1331	–	–	βr HCO[67]
1378	1335	1.35	184.37	1370	1328	–	–	βr HCC[44]
1371	1328	0.56	96.41	1368	1325	–	1329w	τ HCCH[42]
1355	1313	0.08	141.22	1356	1314	–	1310w	β HCC on ring[50]
1342	1300	0.61	44.71	1335	1294	–	–	β HCC of CH_3 on ring[53]
1329	1288	1.10	35.85	1328	1286	–	–	βr HCC[60]
1315	1274	2.77	31.16	1311	1270	–	1273w	βr HCC[51]
1306	1266	2.44	133.44	1298	1257	–	–	βr HCC[68]
1272	1233	16.17	94.39	1272	1232	1237vs	1240w	βr HCC[58]
1265	1225	51.61	152.48	1261	1222	–	–	βd CH_2 on ring[48]
1256	1217	390.67	57.65	1222	1183	–	1217w	β HCC on ring[35] +υ C–O[31]
1202	1165	5.39	78.96	1204	1166	1182w	1182w	υ CC[36]
1199	1162	9.66	197.36	1199	1162	1160w	1153w	υ CC[12]
1183	1146	5.03	62.98	1182	1146	–	–	τ HCCH[44]
1169	1133	3.50	204.46	1167	1130	–	–	β HCC[40]
1122	1087	2.74	63.81	1119	1084	1097w	1101w	υ CC[14]
1108	1074	14.44	76.89	1103	1069	–	1080w	υ CC[40]
1094	1060	7.83	122.62	1090	1056	–	1059w	υ CC[32]
1071	1038	1.51	86.37	1068	1035	–	1040w	υ CC on ring[36]+β HCC [24]
1064	1031	4.95	2.04	1064	1031	1023s	–	β HCC of CH_3^{IV}[74]
1047	1015	22.72	265.44	1040	1008	–	1011w	υ CC[50]
1038	1005	133.35	73.55	1016	984	–	–	β HCC of CH_3^{IV}[49]+υ C–O[11]
1016	985	3.16	112.50	1006	975	982w	978w	υ CC on ring [39]
990	959	14.07	137.26	991	960	965w	957w	υ CC on ring [47]
983	952	4.79	173.18	988	958	–	–	υ CC[25]
971	941	13.93	89.22	979	948	–	932w	υ C–O[35]
965	935	1.71	130.19	967	937	–	–	β HCC[45] + υ CC[10]
937	908	1.32	185.48	943	914	–	–	υ CC[49]
933	904	0.87	31.96	938	909	904w	905w	β HCC on CH_3^{III}[39]
929	900	1.03	42.93	930	901	–	–	β HCC on isopropyl[55]
918	889	9.40	138.05	889	861	–	876w	υ CC[21]+β HCC on ring[16]
879	851	0.67	213.19	872	845	842w	843w	υ CC[57]
850	823	6.34	49.30	818	793	805w	808w	τ HCCC[21]+υ CC[13]
810	785	0.31	124.77	806	781	776w	775m	υ CC[47]+τ HCCC[47]
777	753	0.03	565.98	783	759	697w	741w	υ CC[40]
652	632	4.19	281.30	628	609	651w	652w	υ C–O[32]+υ CC[28]
613	594	7.09	68.85	601	582	609w	598w	τ CCOC[56]+β HCC[10]
594	575	0.71	76.09	601	582	564w	569w	τ HCCC[32]+τ CCOC[12]+υ CC[11]
538	522	1.00	410.68	538	521	538w	540w	τ HCCC[30]
507	491	4.58	91.95	511	495	477m	500w	τ CCCC[36]
479	464	3.76	114.48	500	485	460m	465w	β CCC[62]
464	449	1.58	84.74	465	451	–	442w	β CCC[60]

Table 7. Comparison between Experimental and Computed Vibrational frequencies of IR and Raman spectra for RMA with assignments and PED % (Continued)

Frequencies (cm^{-1})								
Computed						Experimental		Assignments [PED%]
Conformer (g1)				Conformer (g2)				
υ_{un}	υ_{sc}*	I_{IR}	I_{Raman}	υ_{un}	υ_{sc}*	IR	Raman	
434	421	0.40	96.67	447	433	408s	407w	β CCC[57]
407	394	0.21	416.30	412	399	–	–	β CCC[50]
393	381	0.94	148.29	398	385	–	–	τ CCCC[52]
307	298	1.73	838.88	353	342	–	315w	τ HCCC[26]
288	279	0.44	287.69	297	288	–	291w	τ HCCC[24]+τ HCCC[13]
283	274	1.39	270.04	293	284	–	262w	τ HCCC[24]+τ HCCC[12]
258	249	1.54	282.04	287	278	–	–	β CCC[46]
238	230	0.25	30.89	274	266	–	–	τ HCCC[38]+τ HCCC[10]
234	227	0.17	48.30	272	264	–	228w	τ HCCC[43]+τ HCCC[17]
222	215	0.13	17.58	264	255	–	–	τ HCCC[43]+τ HCCC[21]
216	209	1.07	47.68	238	231	–	–	τ HCCC[32]+τ HCCC[14]
199	192	3.10	83.13	235	227	–	178w	τ CCCC[37]+τ HCCC[10]+τ HCCC[10]
165	160	0.47	195.34	224	217	–	–	τ CCOC[40]+β HCC[11]
107	104	1.64	193.09	177	171	–	–	τ CCOC[40]
81	79	1.57	1223.72	125	122	–	72s	τ COCC[42]+τ HCCO[31]
68	65	0.03	208.20	112	108	–	–	τ CCCC[59]
47	46	0.13	2345.13	80	77	–	–	τ HCCO[52]+τ CCCO[13]
43	41	0.24	6388.43	72	70	–	–	τ HCCO[46]+τ COCC[33]
38	37	2.55	7592.41	68	66	–	–	τ HCCO[64]

Note: I_{IR} = Computed IR intensities in km/mole, I_{Raman} = Computed Raman intensities.
CH_3^{I} = Methyl group at ortho position, CH_3^{II} = Methyl group at meta position, CH_3^{III} &CH_3^{IV} = Methyl groups at para position of RMA ring.
Intensities of experimental bands are described as vs= very strong, s=strong, m=medium, w=weak. Modes description: υ = stretching, υas = asymmetric stretching, υs= symmetric stretching, β = bending, βs = scissoring, βr = rocking, γ = out of plane bending, γw= wagging, βd = deformation and τ = torsion.
υ_{un} = Unscaled frequencies (cm^{-1}) and υ_{sc}* = Scaled frequencies (cm^{-1}).
* = Scaled frequencies using scaling factor 0.9688 [7].

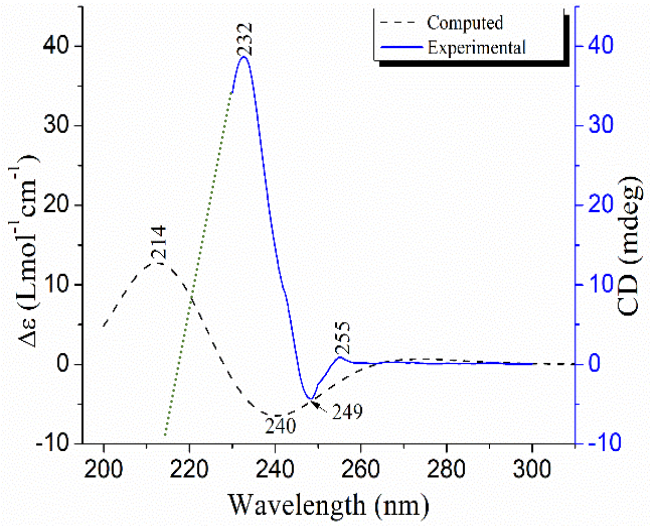

Figure 8. Comparison of the experimental ECD spectrum of RMA in chloroform with the computed ECD spectrum (dashed line) using the IEFPCM solvation model at the B3LYP/6-311++G(d,p) level. The orange dotted line represents the extrapolated continuation of the measured spectrum below 230 nm

3.4. UV−Vis and ECD analyses

The UV−Vis absorption characteristics of RMA experimental spectrum, recorded in chloroform (see Figure 7), exhibits three absorption peaks at 219, 241 and 276 nm, corresponding to $\pi\rightarrow\pi^*$ (219 nm) and $n\rightarrow\pi^*$ (241 and 276 nm) transitions typically associated with ester group. *The weak absorption at 219 nm is attributed to a* $\pi\rightarrow\pi^*$ transition, with its low intensity indicating a weakly allowed transition, due to limited orbital overlap or a low transition probability.

The electric field vector of incident light couples weakly with the transition dipole moment here, leading to diminished absorbance.

Additionally, steric hindrance or conformational locking by the menthyl group may reduce orbital delocalization, further suppressing this transition. In contrast, the sharp and intense band at 241 nm corresponds to a $n\rightarrow\pi^*$ transition localized on the ester carbonyl group. This is a

strongly allowed transition, where the incident electromagnetic radiation couples efficiently with the electric dipole moment associated with the lone pair and π^* antibonding orbitals in the carbonyl group. The high intensity and sharp nature suggest minimal vibrational coupling, indicating a rigid local environment, stabilized by the C–H···O H–bonding.

The strong electronic polarization and efficient energy gap alignment make this transition highly probable.

The electric field of the light interacts directly with the electron cloud movement in the π system, maximizing absorption.

The broader and relatively intense band at 276 nm is assigned to an $n\rightarrow\pi^*$ transition involving the lone pair on the oxygen of the carbonyl is promoted to the π^* orbital of the carbonyl group.

The intense, broadened band at 276 nm corresponds to $n \rightarrow \pi^*$ transition, typically magnetic−dipole allowed but electric−dipole weak. Inhomogeneous broadening, caused by variations in the carbonyl environment (e.g., C–H···O interactions), leads to energy dispersion. Enhanced n–π^* overlap via lone pair delocalization and local anisotropic fields further amplify the transition's intensity.

Further, its high intensity and broadening are influenced by solvent effects, indicating electronic perturbations that may contribute to electronically anharmonic behaviorTo support these assignments, TD−DFT calculations were carried out at the B3LYP/6−311++G(d,p) level using the IEFPCM solvation model for chloroform.

The computed UV spectrum shows wavelengths 214, 239 and 258 nm, in good agreement with the experimental data. The calculated 214 nm transition (2.28% deviation) corresponds to a $\pi\rightarrow\pi^*$ excitation localized over the ester carbonyl and adjacent carbon atoms, as detailed in Table 8 and 8a. Similarly, the computed 239 nm peak (0.83% deviation) aligns well with the experimental 241 nm band, reflecting an $n\rightarrow\pi^*$ transition involving enhanced electronic delocalization across the ester group

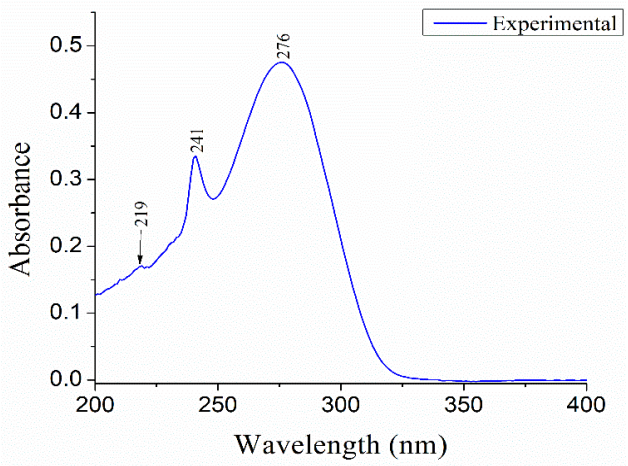

Figure 7. Experimental UV−Vis spectrum of RMA (0.1 mM) in chloroform, showing absorbance against wavelength (nm)

Table 8. Experimental and computed UV−Vis absorption data of RMA. Theoretical wavelengths were obtained using DFT at B3LYP/6−311++G(d,p) level. Computed values were converted to wavenumbers (cm^{-1}), scaled by a factor of 0.9688 and converted back to wavelengths (nm) to account for systematic overestimation in TD−DFT calculations [7, 47, 48]

State	Experimental		Computed				
	λ (nm)	Energy (eV)	λ (nm)	Energy (eV)	Oscillatory Strength, f	Dominant Transition	Transition
1	276	4.49	258	4.81	0.0013	55 → 57	$n \rightarrow \pi^*$
2	241	5.15	239	5.19	0.0284	55 → 56	$n \rightarrow \pi^*$
3	219	5.66	214	5.81	0.0631	54 → 56	$\pi \rightarrow \pi^*$

Table 8a. Comparison of experimental and calculated UV and ECD spectral bands of RMA, showing absolute (**Δλ**) and percentage errors (**δ%**) along with the assigned electronic transitions

E_{UV} (nm)	C_{UV} (nm)	Δλ (E_{UV} — C_{UV}) (nm)	δ% E_{UV} to C_{UV}	E_{CD} (nm)	C_{CD} (nm)	Δλ (E_{CD} — C_{CD}) (nm)	δ% E_{CD} to C_{CD}	δ% E_{UV} to E_{CD}	Transitions
276	258	18	6.52	255 (+)	—	—	—	7.61	$n\rightarrow\pi^*$
241	239	2	0.83	232 (+) 249 (–)	214 (+) 240 (–)	18 9	7.75 3.61	3.73 3.31	$n\rightarrow\pi^*$
219	214	5	2.28	—	—	—	—	—	$\pi\rightarrow\pi^*$

Note: E_{UV} = Experimental UV, C_{UV} = Computed UV, E_{CD} = Experimental ECD and C_{CD} = Computed ECD.
(+) = Positive Cotton effect and (–) = Negative Cotton.

10.57647/jtap.2026.2002.11

However, the calculated 258 nm transition shows a larger deviation from the experimental 276 nm band (6.52%), likely due to conformational flexibility or long−range interactions.

This weakly allowed $n\rightarrow\pi^*$ transition, with a low oscillator strength (f = 0.0013), originates from the lone pair orbital on the carbonyl oxygen. Such deviations are consistent with the known limitations of TD–DFT, where accuracy strongly depends on the chosen functional and solvation model; at the B3LYP/6-311++G(d,p) level, it may underestimate weakly allowed or solvent–sensitive excitations and misrepresent charge-transfer or double-excitation states.

The UV−Vis $\pi\rightarrow\pi^*$ and $n\rightarrow\pi^*$ transitions of the carbonyl group correlate with the deshielding effects observed in the ^{1}H NMR spectrum.

The carbonyl group's anisotropic shielding cone and electron−withdrawing nature influence nearby proton environments, particularly the equatorial protons on the menthyl ring.

The C5–H12···O36 H–bonding between a ring proton and the carbonyl oxygen further enhances deshielding by reducing electron density around the involved C5–H12 bond.

Electronic transitions reflect the molecule's electron distribution and when lone pairs or π systems are involved, they reduce local shielding, causing NMR protons to shift downfield.

These effects stabilize specific conformers, as reflected in the sharp $n\rightarrow\pi^*$ transition at 241 nm, while the $n\rightarrow\pi^*$ band at 276 nm indicates lone−pair polarization with broadening, consistent with the H–bonding interactions observed in the NMR spectrum.

The electronic transitions observed in the UV−Vis spectrum are further elucidated by the ECD data. The ECD spectrum shows a strong positive Cotton effect at 232 nm, which aligns closely with the medium−intensity $n\rightarrow\pi^*$ absorption at 241 nm in the UV spectrum. The slight blue shift (deviation 3.73%) can be attributed to differences in chiroptical sensitivity.

The positive sign of the Cotton effect at this position indicates the excitation of left−circularly polarized light by the chiral π−system, meaning that the asymmetric environment comprising the chiral center and rigid cyclohexane ring affects the orientation of the electronic transition dipole.

The weaker negative Cotton effect at 249 nm and the positive Cotton effect at 255 nm correspond to strong UV bands at 241 and 276 nm, respectively, both assigned to $n\rightarrow\pi^*$ transitions.

This inverse intensity pattern between ECD and UV bands reflects the nature of rotational strength, which depends on the orientation and coupling of electric and magnetic transition dipole moments. Supporting these assignments, TD−DFT calculations predict a positive Cotton effect at 214 nm and a negative one at 240 nm, in good agreement with experimental observations.

Overall, the spectral data confirm that the chiroptical response is strongly governed by the electronic transition character and the alignment of transition moments in the chiral environment of the molecule.

This overlap underscores that $n\rightarrow\pi^*$ transitions, although weak in conventional absorption, can become optically active in a chiral, rigid environment such as RMA [29].

3.4.1. *Frontier molecular orbital analysis*

The TD−DFT analysis shows that the electronic transitions in RMA occur mainly between the HOMO and LUMO, consistent with Frontier Molecular Orbital (FMO) theory, which helps to explain the molecule's electronic and optical behavior [30, 31].

This theory indicates that the HOMO functions as a nucleophilic electron donor and the LUMO as an electrophilic acceptor [18].

The HOMO–LUMO energy gap (ΔE) indicates molecular stability and reactivity: a larger ΔE suggests greater stability and lower reactivity, while a smaller ΔE implies higher reactivity and reduced stability.

The FMO−based analysis of electronic excitations in RMA and the corresponding HOMO–LUMO energy levels are shown in Figure 9.

In RMA, three main electronic transitions were identified: 55→57 ($n\rightarrow\pi^*$) at 276 nm, 55→56 ($n\rightarrow\pi^*$) at 241 nm and 54→56 ($\pi\rightarrow\pi^*$) at 219 nm. The associated excitation energies range from 7.541 to 7.701 eV.

These transitions involve orbitals localized mainly around the carbonyl ester and hydrocarbon chains, showing significant electron redistribution from lone pairs on oxygen atoms and π−system into π^* orbitals upon excitation.

The computed HOMO–LUMO gap is ~7.6 eV indicates high electronic stability and low chemical reactivity.

This value implying that RMA is more electronically rigid and less likely to undergo photochemical changes [18].

Orbital visualizations further support these findings: red and green colorations in the plots denote positive and negative orbital phases, respectively, facilitating analysis of charge−transfer characteristics.

These theoretical results are good agreement with experimental UV spectra, highlighting the significance of the HOMO–LUMO gap, orbital character andtransition nature in the photophysical properties of RMA [32].

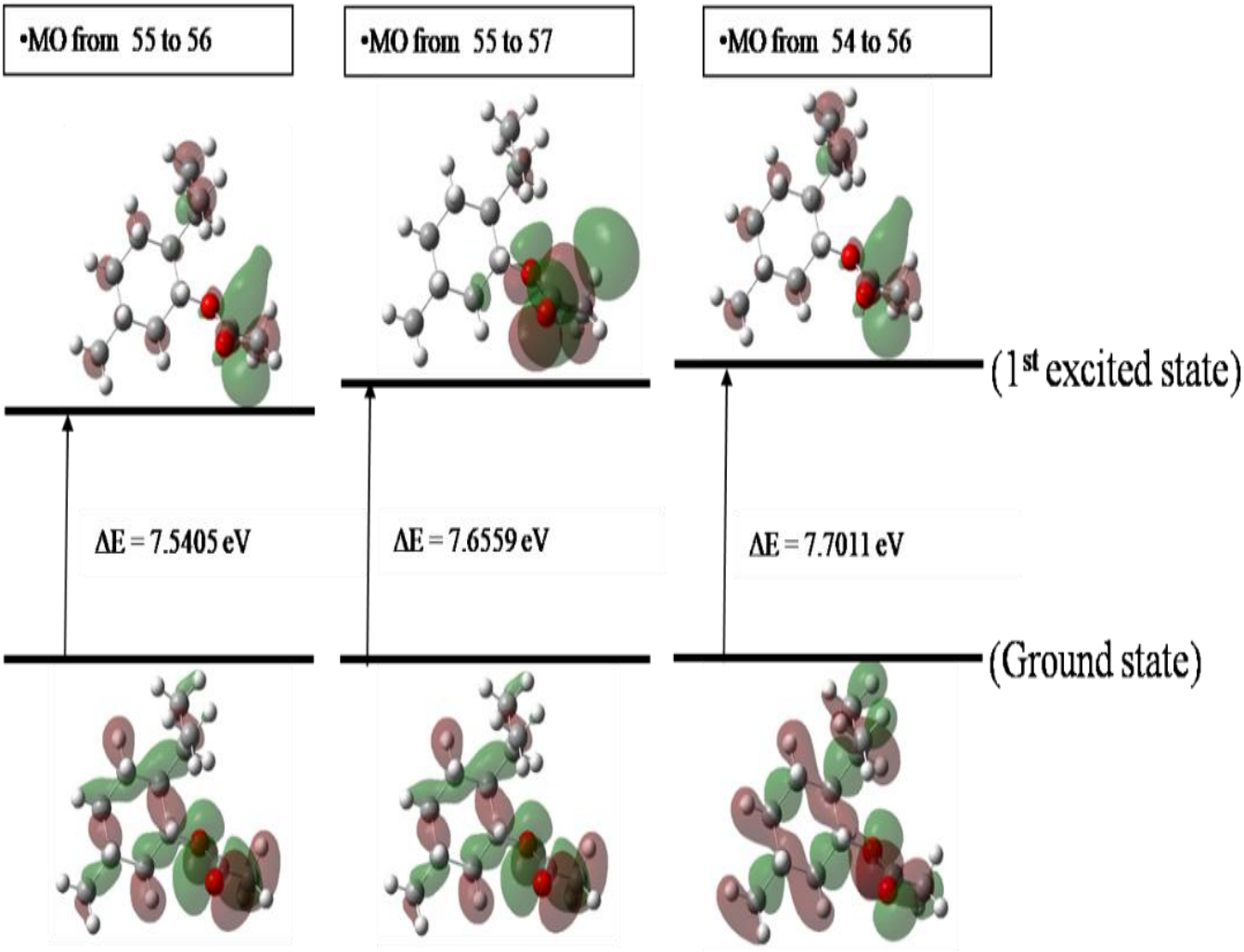

Figure 9. Visualization of selected molecular orbitals (MOs) of RMA, computed at B3LYP/6−311++G(d,p) level. The highlighted orbitals represent HOMO–1 (MO 54), HOMO (MO 55), LUMO (MO 56) and LUMO+1 (MO 57). The calculated energy gaps for the electronic transitions are 7.5405 eV (55→56), 7.6559 eV (55→57) and 7.7011 eV (54→56), indicating a relatively large excitation energy

3.5. Natural bonding orbital analysis

To support the NMR−based evidence for intra−molecular C–H···O H–bonding in RMA, a detailed NBO analysis was conducted using DFT method at B3LYP/6−311++G(d,p) level [9−14,33,34].This analysis provides information on the molecule's electronic structure, especially regarding charge separation and donor–acceptor interactions relevant to non−covalent C–H···O bonding. The natural charges obtained from the NBO analysis show significant electronic polarization centered on the ester functional group. That is the carbonyl oxygen (O36) and alkoxy oxygen (O30) shows negative charges (−0.606 e and −0.580 e, respectively), indicating strong lone−pair electron density that confirms these atoms to act as H–bond acceptors. The carbonyl carbon (C31), with a positive charge of +0.810 e, underscores the electrophilic character of the ester, while the adjacent carbon (C32, −0.666 e) further enhances local polarization.

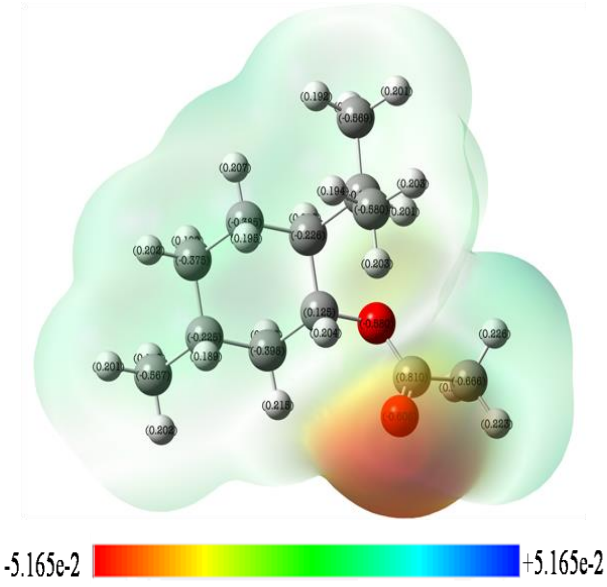

Figure 10. Molecular Electrostatic Potential surface of RMA computed at B3LYP/6−311++G(d,p) level. The color scale (Red to Blue) ranges from –0.05165 to 0.05165 a.u.

n(2)O36→π*(C31−O36), $E^{(2)}$ = 47 kcal/mol

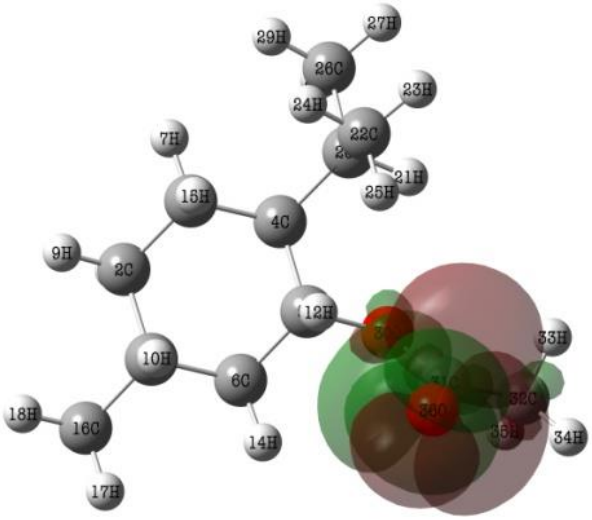

n(2)O36→σ*(O3O−C31), $E^{(2)}$= 32 kcal/mol

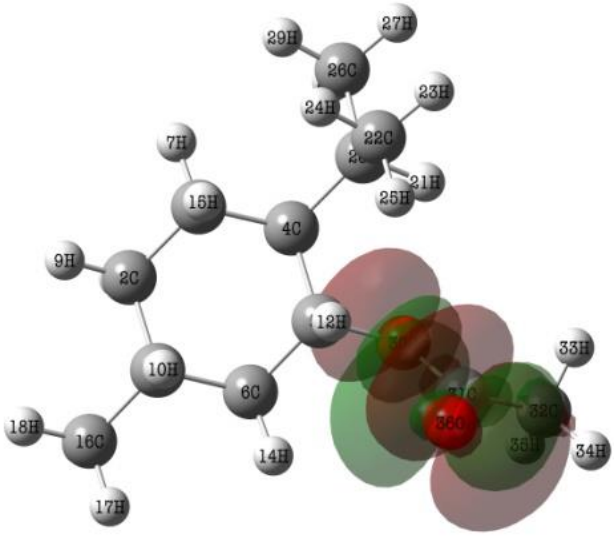

n(2)O36→σ*(C31−C32), $E^{(2)}$ = 18 kcal/mol

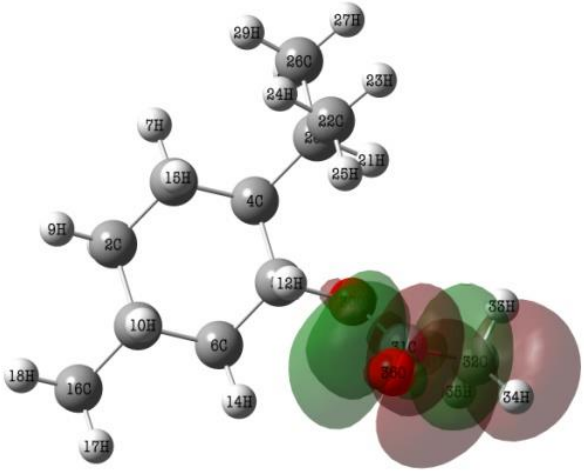

n(1)O30→σ*(C31−O36), $E^{(2)}$ = 8 kcal/mol

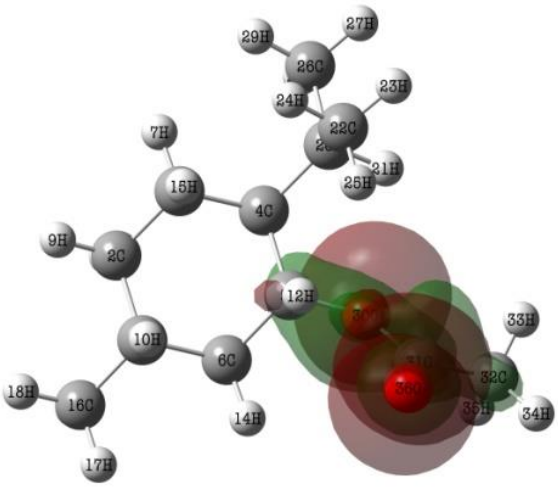

π(C31−O36)→π*(C31−O36), $E^{(2)}$=0.71 kcal/mol

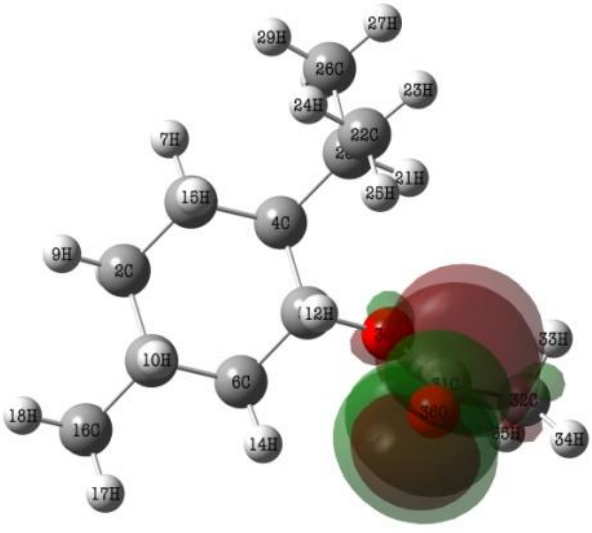

n(2)(O36)→σ*(C5−H12), $E^{(2)}$=0.52 kcal/mol

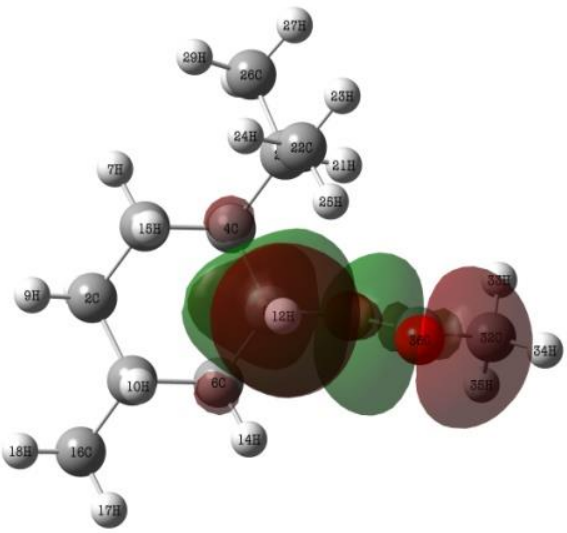

Figure 11. NBO donor–acceptor interactions in RMA showing C−H···O, n–π*, n–σ* and π–π* delocalizations with corresponding stabilization energies ($E^{(2)}$, kcal/mol)

10.57647/jtap.2026.2002.11

Table 9. Natural atomic charges derived from NBO analysis, highlighting electron−rich and electron deficient sites across the molecular structure of RMA

Atom	Charge (a.u.)	Atom	Charge(a.u.)
C1	−0.22500	H19	0.19451
C2	−0.37532	C20	−0.22693
C3	−0.38513	H21	0.20121
C4	−0.22649	C22	−0.57974
C5	0.12501	H23	0.20252
C6	−0.39802	H24	0.19418
H7	0.20703	H25	0.20269
H8	0.19027	C26	−0.56922
H9	0.20199	H27	0.20141
H10	0.18942	H28	0.19912
H11	0.19978	H29	0.19237
H12	0.20418	O30	−0.58032
H13	0.19823	C31	0.81038
H14	0.21546	C32	−0.66581
H15	0.19529	H33	0.22581
C16	−0.5669	H34	0.22342
H17	0.20231	H35	0.22726
H18	0.20099	O36	−0.60598

Hydrogen atoms generally exhibit expected small positive charges (~+0.20 e), while most carbons in the saturated menthyl skeleton range from −0.38 to −0.56 e, except for chiral center C5 (+0.125 e), which is slightly electron deficient due to its connectivity with oxygen and hydrogen atoms. These charge distributions highlight the polar nature of the ester group, identifying O36 as a dominant electron rich center, C31 as a reactive electrophilic site and highlighting potential reactive centers for nucleophilic interactions through C–H···O bonding. This charge distribution agrees with the observed downfield shifts in the proton NMR spectrum, confirming the presence of weak but directionally significant C–H···O interactions. The computed Molecular Electrostatic Potential (MEP) surface of RMA, shown in Figure 10, visualizes the charge distribution based on natural population analysis (NPA) at the B3LYP/6−311++G(d,p) level, where red regions denote areas of higher electron density and blue regions indicate electropositive regions, consistent with the NPA−derived atomic charges listed in Table 9. According to Second−order perturbation theory analysis of the NBO, the most dominant interaction arises from the lone pair donation on the carbonyl oxygen, n(2)O36, into the π^*(C31–O36) antibonding orbital, with a stabilization energy of ~47 kcal/mol. This strong n–π^* delocalization reinforces the partial double bond character of the ester group and reduces the shielding of adjacent nuclei, thus accounting for the downfield shifts observed in the NMR spectrum due to anisotropy. A π–π^* interaction within the same bond [π(C31–O36)→π^*(C31–O36)] was also observed, though with a weak stabilization energy of 0.71 kcal/mol, indicating that the dominant delocalization arises from lone pair donation rather than classical bond resonance [35]. The corresponding NBO orbitals and their associated stabilization energies are illustrated in Figure 11. Further significant interactions included n(2)O36→σ^*(C31–O30) with ~32 kcal/mol and n(2)O36→σ^*(C31–C32) with ~18 kcal/mol, illustrating extensive hyperconjugative overlap between the carbonyl oxygen and neighboring ester group. These n–σ^* interactions further stabilize the planar geometry of the ester group and support the partial double bond character of the C=O and C–O bonds. Additionally, the alkoxy oxygen (O30) also acted as a donor, with n(1)O30→σ^*(C31–O36) and n(2)O30→σ^*(C5–C6) interactions contributing ~8 kcal/mol and ~5 kcal/mol, respectively. Further, a weak n(2)(O36)→σ^*(C5–H12) interaction with 0.52 kcal/mol stabilization energy was identified, indicating minor stabilization through a C–H···O contact.

3.6. QT−AIM analysis

3.6.1. *Topological parameters*

To explore the structural and electronic properties of the RMA molecule, a topological analysis was performed based on Bader's QT−AIM theory. The identification of

BCPs and RCPs confirmed the presence of weak C–H···O bonds, van der Waals and steric interactions. These features support the observed NMR chemical shift variations arising from anisotropy and intra−molecular interaction, and further validate NBO−predicted electron delocalization. The RCPs also indicates the stable cyclohexane chair conformation of RMA. Topological parameters including electron density (ρ(r)), its Laplacian ($\nabla^2\rho(r)$), energy densities (kinetic energy density (G(r)), potential energy density (V(r)), total energy density (H(r)=G(r)+V(r)), interaction energy (E_{int}) and binding energy (E_{BE}) were computed to characterize these interactions, as shown in Figure 12 and tabulated in Table 10. Covalent interactions within the molecular structure, particularly those involving C–C and C–H bonds, exhibit high ρ(r) values (0.222–0.272 a.u.) and negative Laplacians (–0.516 to –0.809 a.u.), signifying electron−sharing interactions. These features are further supported by negative interaction energies, such as those observed in the C4–C5 (–84.47 kcal/mol) and C5–C6 (–85.03 kcal/mol) bonds, indicates localized bonding characteristic of the molecular core.

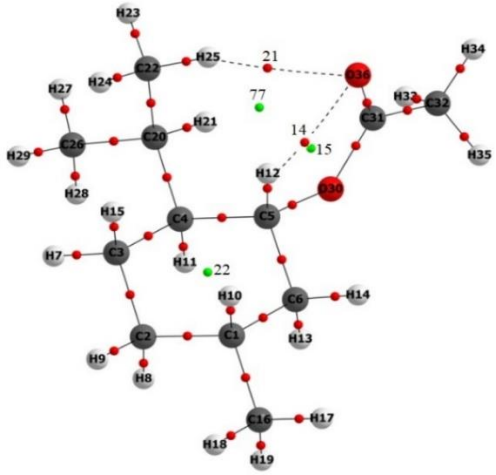

Figure 12. RMA molecular structure containing (a) Bond Critical Points (BCPs) (Red dots), H−bonded BCPs indexed as 14 (H12···O36) and 21 (H25···O36), (b) Ring Critical Points (RCPs) (green dots), indexed as 22 (C1−C2−C3−C4−C5−C6), 15 (C5−O30−C31−O36−H12) and 77 (H25−C22−C20−C4−C5−H12−O36)

Table 10. Topological parameters corresponding to Bond Critical Points (BCPs) and Ring Critical Points (RCPs) for RMA

Atoms	BCP index	ρ(r) in a.u.	$\nabla^2\rho(r)$ in a.u.	G(r) in a.u.	K(r) in a.u.	V(r) in a.u.	H(r) in a.u.	E_{int} in (kcal/mol)	E_{BE} in (kcal/mol)
C1 − C2	20	0.225639	−0.545646	0.061021	0.197432	−0.258453	−0.197432	−81.0909	−49.593
C2 − C3	26	0.222964	−0.534867	0.060054	0.193770	−0.253824	−0.193770	−79.63858	−48.997
C4 − C5	23	0.231757	−0.569134	0.063464	0.205748	−0.269211	−0.205748	−84.46642	−50.958
C3 − C4	29	0.222256	−0.528087	0.060624	0.192646	−0.253270	−0.192646	−79.46472	−48.839
C3 − H7	35	0.259749	−0.746765	0.048119	0.234810	−0.282929	−0.234810	−88.77029	−57.203
C1 − C6	10	0.224083	−0.538502	0.060964	0.195589	−0.256553	−0.195589	−80.4948	−49.246
C5 − C6	16	0.232971	−0.582499	0.062685	0.208309	−0.270994	−0.208309	−85.02574	−51.229
C6 − H14	2	0.258939	−0.742670	0.047412	0.233079	−0.280491	−0.233079	−88.00553	−57.022
C2 − H8	25	0.257020	−0.731828	0.048320	0.231277	−0.279597	−0.231277	−87.72493	−56.594
C2 − H9	24	0.258053	−0.739070	0.047837	0.232604	−0.280441	−0.232604	−87.98987	−56.824
C1 − H10	8	0.258472	−0.737636	0.048561	0.232970	−0.281532	−0.232970	−88.33196	−56.918
C4 − H11	30	0.258684	−0.736231	0.048649	0.232707	−0.281356	−0.232707	−88.27695	−56.965
C3 − H15	27	0.258302	−0.737917	0.048575	0.233054	−0.281629	−0.233054	−88.36249	−56.88
C6 − H13	12	0.258551	−0.738617	0.047592	0.232246	−0.279839	−0.232246	−87.80078	−56.935
C1 − C16	7	0.224585	−0.544229	0.060262	0.196320	−0.256582	−0.196320	−80.50386	−49.358
C16 − H18	3	0.257174	−0.737136	0.047417	0.231701	−0.279119	−0.231701	−87.57486	−56.628
C16 − H17	1	0.257134	−0.736832	0.047434	0.231642	−0.279076	−0.231642	−87.56147	−56.619
C16 − H19	5	0.256696	−0.733710	0.047622	0.231049	−0.278671	−0.231049	−87.43442	−56.522
C4 − C20	31	0.220668	−0.516718	0.059312	0.188491	−0.247803	−0.188491	−77.7495	−48.484
C20 − C26	37	0.223192	−0.536662	0.059797	0.193963	−0.253760	−0.193963	−79.61843	−49.047
C20 − H21	32	0.261374	−0.752421	0.048393	0.236498	−0.284891	−0.236498	−89.38604	−57.565
C20 − C22	33	0.222289	−0.531989	0.059724	0.192721	−0.252444	−0.192721	−79.2057	−48.846
C22 − H23	36	0.256179	−0.730372	0.048429	0.231022	−0.279451	−0.231022	−87.679	−56.406

Table 10. Topological parameters corresponding to Bond Critical Points (BCPs) and Ring Critical Points (RCPs) for RMA (Continued)

Atoms	BCP index	ρ(r) in a.u.	∇2ρ(r) in a.u.	G(r) in a.u.	K(r) in a.u.	V(r) in a.u.	H(r) in a.u.	Eint in (kcal/mol)	EBE in (kcal/mol)
C22 − H24	34	0.256623	−0.732052	0.048899	0.231912	−0.280810	−0.231912	−88.10566	−56.505
C26 − H27	40	0.257190	−0.736432	0.047800	0.231908	−0.279708	−0.231908	−87.75991	−56.632
C26 − H29	39	0.257464	−0.737035	0.048246	0.232505	−0.280751	−0.232505	−88.08708	−56.693
C26 − H28	38	0.256529	−0.733554	0.047838	0.231226	−0.279064	−0.231226	−87.55763	−56.484
C5 − O30	19	0.192501	−0.092567	0.122726	0.145868	−0.268594	−0.145868	−84.27282	−42.201
C32 − H35	4	0.258364	−0.742911	0.045617	0.231344	−0.276961	−0.231344	−86.89785	−56.894
O30 − C31	13	0.255639	−0.251075	0.165594	0.228363	−0.393957	−0.228363	−123.6058	−56.286
C31 − O36	11	0.371286	−0.418837	0.398579	0.503289	−0.901868	−0.503289	−282.9656	−82.084
C31 − C32	9	0.236194	−0.573512	0.070792	0.214171	−0.284963	−0.214171	−89.40854	−51.948
C32 − H34	6	0.262515	−0.762903	0.045670	0.236396	−0.282066	−0.236396	−88.49971	−57.819
C32 − H33	17	0.257307	−0.738289	0.045554	0.230126	−0.275680	−0.230126	−86.49603	−56.658
H−Bonds Regions (C5−H12···O36 and C22−H25···O36)									
C5 − H12	18	0.271164	−0.809401	0.040853	0.243203	−0.284055	−0.243203	−89.12378	−59.749
H12 − O36	14	0.020144	0.090949	0.021093	−0.00164	−0.019449	0.001644	−6.102289	−3.7514
C22 − H25	28	0.260682	−0.753404	0.045848	0.234199	−0.280047	−0.234199	−87.86628	−57.411
H25 − O36	21	0.010745	0.051901	0.010401	−0.00258	−0.007826	0.002575	−2.455457	−1.6546

RCP index	Atom count	ρ(r) in a.u.	$\nabla^2\rho(r)$ in a.u.	K(r) in a.u.	G(r) in a.u.	V(r) in a.u.	H(r) in a.u.	E_{int} in (kcal/mol)	E_{BE} in (kcal/mol)
22	6	0.019976	0.092348	−0.001571	0.021516	−0.01994	0.00157132	−0.00997	−3.71395
15	5	0.020131	0.095806	−0.001901	0.022051	−0.02015	0.00190054	−0.01008	−3.74852
77	7	0.007091	0.032113	−0.001939	0.00609	−0.00415	0.00193856	−0.00208	−0.83956

Note: ρ(r)= Electron density, $\nabla^2\rho(r)$ = Laplacian of electron density, K(r) = Total Kinetic energy density, G(r) = Lagrangian Kinetic energy density, V(r) = Potential energy density, H(r) = Total energy density, E_{int} = Interaction energy and E_{BE} = Binding Energy

The C5–H12···O36 bonding in RMA is influenced by the electronic environment created by nearby covalent bonds. The C5–H12 bond, part of the rigid cyclohexane ring, is a strong localized covalent bond that polarizes H12, making it slightly electropositive as seen in NBO analysis. In contrast, The C31–O36 bond is especially for its high electron density (0.3713 a.u.), large interaction energy (–282.97 kcal/mol) and strong delocalization, enhancing O36 ability to act as a H–bond acceptor.

This electron−rich O36 interacts with the polarized H12 through a weak but directional C–H···O bond.

The combined influence of these covalent bonds stabilizes this non−covalent contact, contributing to conformational rigidity and supporting the observed NMR deshielding of H12. This electron delocalization is further visualized by using the ELF and LOL analyses.

In contrast to this C5−H12···O36 bonding, the analysis shows another weak intra−molecular C22−H25···O36 H−bond. These contact is distinguished by its low electron densities 0.0107 a.u. and positive Laplacian 0.0519 a.u.), showing interactions dominated by closed−shell, non−covalent character. The both H−bonds of H12···O36 and H25···O36, exhibit interaction/binding energies of –6.10/–3.75 and –2.46/–1.65 kcal/mol, respectively, further indicates their weak stabilizing molecular interactions. The RCPs indexed 15 and 77 (as shown Figure 12), were identified along non−covalently enclosed paths are associated with van der Waals interactions. The corresponding ρ(r) values at these RCPs (0.0201 and 0.0071 a.u.) along with small but positive Laplacians (0.0958 and 0.0321 a.u.) highlight regions of diffuse electron accumulation. These features are reflecting of van der Waals interactions, further supported by extremely low interaction energies (–0.010 and –0.002 kcal/mol) and binding energies (–3.74 and –0.83 kcal/mol).

Similarly, RCP 22 highlights steric interaction at the ring center of RMA.

Thus, the analysis shows a dual interaction model comprising covalent and non−covalent interactions including H–bonding, steric and van der Waals interactions which are clearly visualized in RDG maps obtained from NCI and IRI analyses, as discussed further below

3.6.2. *NCI analysis*

Non−covalent interactions in RMA were characterized using NCI and RDG analyses (Figure 13), which clearly shows weak intra−molecular forces playing a pivotal role in stabilizing its compact chair conformation. The RDG vs. sign(λ_2)ρ plot, along with isosurfaces mapped on the molecular structure, identifies three key interaction types (H−bonds, van der Waals and steric interactions) that define the molecule's non−covalent framework [10, 11, 13, 14, 36−38].The central green region of the scatter plot, around sign(λ_2)ρ ≈ 0.000 a.u., corresponds to low electron density zones (ρ < 0.01 a.u.) dominated by van der Waals interactions. These interactions are significant, as indicated by the broad and dense RDG distribution within the range 0.00 to –2.00 a.u. The green isosurfaces in the molecular structure highlight regions of weak, attractive dispersive forces primarily between the equatorial methyl and isopropyl groups surrounding the cyclohexane ring, as shown in Figure 13.

such weak forces, although energetically modest, act cooperatively to maintain the low−energy, rigid chair structure of RMA.

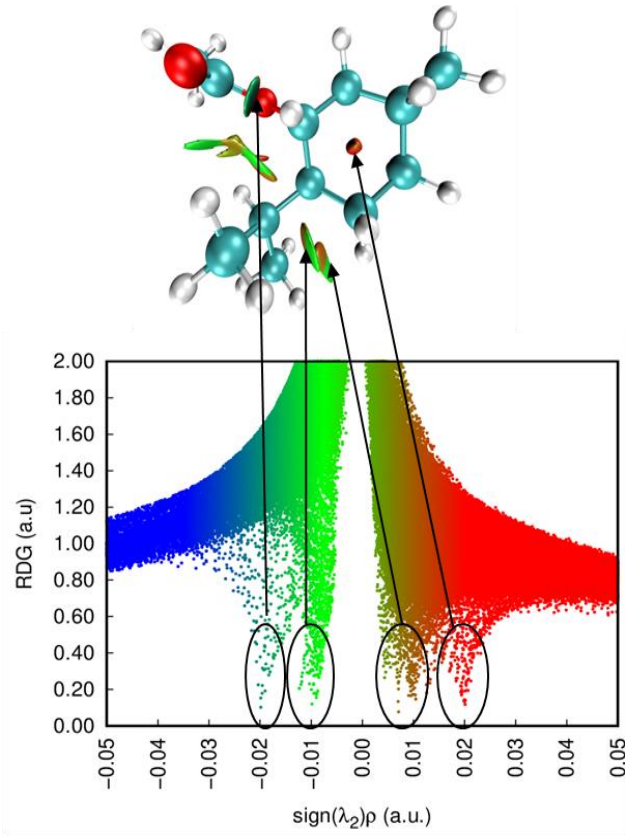

Figure 13. (a) Reduced density gradient isosurface for RMA. Steric interaction (indicated by red color at the centre of the ring), van der Waals interaction (shown in green color between neighboring within monomer) and H−bond (C−H···O) interaction (blue colored) but it is weaker in this molecule. (b) Scatter plot of RDG versus sign(λ_2)ρ for RMA. The circles positioned on the lower troughs below the dotted horizontal line (at iso value 0.5) illustrate the NCI interactions

The conformational rigidity induced by van der Waals and steric constraints ensures that the chiral environment around the chromophore remains fixed, thereby enforcing a consistent Cotton effect in the ECD spectrum. This indicates that the non−covalent framework does not just stabilize geometry but also affects optical activity through restricted rotational freedom around the ester group. On the right−hand side of the RDG plot, red regions (sign(λ_2)ρ> +0.010 a.u., RDG = +0.2 to +1.6 a.u.) reflect steric repulsions, particularly between the acetate and adjacent axial methyl substituents. These interactions are visualized as red isosurfaces and represent areas of electron cloud crowding that impose conformational boundaries, reducing flexibility and further stabilizing the geometry. This steric hindrance well correlated with NMR observations, where the proton chemical shifts for the C5−H12···O36 and neighboring axial protons show downfield chemical shifts, a result of electron density withdrawal and constrained orientation near carbonyl group.

These shifts confirm the local electronic environments inferred from natural charges derived from NBO analysis. Conversely, on the left side of the RDG plot (sign(λ_2)ρ ≈ −0.010 to −0.030 a.u.), blue regions are sparse, corresponding to H−bonds, such as C5−H12···O36 and C22−H25···O36. These are visualized as faint blue isosurfaces, consistent with low electron density and indicate weak C–H···O bonding in RMA. This suggests such H−bond interactions contribute minimally to conformational stability, although their presence is supported by the deshielded chemical shift observed in the NMR spectrum for C−H···O bonding.

3.6.3. *IRI analysis*

To extend the scope of non−covalent interaction analysis beyond the limitations of NCI plots, the Interaction Region Indicator (IRI) approach was utilized. The IRI and RDG are distinguished solely by a constant pre−factor, denoted as 'a'. fundamentally; IRI is represented by the gradient norm of electron density weighted by scaled electron density [18], expressed in Eq. 1:

$$\text{Interaction Region Indicator, IRI}(r)=\frac{|\nabla\rho(r)|}{[\rho(r)]^{a}} \qquad (1)$$

Here, 'a' serves as an adjustable parameter, with a standard definition value of 1.1. The specific values of 'a' and the constant factor in Eq. 1 are the sole elements differentiating IRI from RDG.

The IRI against sign(λ_2)ρ scatter map, shows the presence of all the interactions presence in RMA molecule, includes covalent, van der Waals, steric interactions and H−bonds. Color codes are as blue region for covalent and H−bonds, red region indicates steric interactions and green region for

van der Waals interactions, as shown in Figure 14, signify these interactions. In the Figure 14(a), the scatter plot presents the IRI values as a function of sign(λ_2)ρ, where λ_2 is the second eigenvalue of the electron density Hessian matrix and ρ is the electron density.

This representations effectively separates interaction types: negative values of sign(λ_2)ρ correspond to attractive interactions, such as covalent bonds and H–bonds, while around zero and positive values indicate van der Waals and steric interactions. The scatter map shows sharp troughs below sign(λ_2)ρ at $|IRI| = 0$, corresponding to strong covalent C–H, C–C, C–O and C=O bonds (at blue region). A central trough near sign(λ_2)ρ = 0 (green colored region) indicates van der Waals interactions. Troughs at 0.01 and 0.02 a.u., where $|IRI| \neq 0$, suggests weak C–H···O bonds, specifically C22–H25···O36 and C5–H12···O36, which are significantly weaker by 91% than covalent bonds in this molecule. Additional troughs above 0.02 a.u. represent steric repulsions. The color coding in the plot distinctly shows these regions: blue for covalent interactions, light blue for weak H–bonds, green for van der Waals interactions and red for steric interactions. The plot also highlights an iso value of 1.0, which serves as a threshold for visualizing interaction regions in the molecular isosurface map. The IRI isosurface map of RMA at the chosen iso value is as shown in Figure 14(b). Here, the spatial distribution of interactions is explicitly illustrated. Blue regions correspond to strong covalent bonds, such as C–C, C–H, C=O and C–O bonds, where electron density is highly localized between atoms. Green regions indicate the presence of van der Waals interactions, which are weaker and more diffuse, typically occurring between non−bonded groups (isopropyl and acetate groups with menthyl ring) in close proximity.

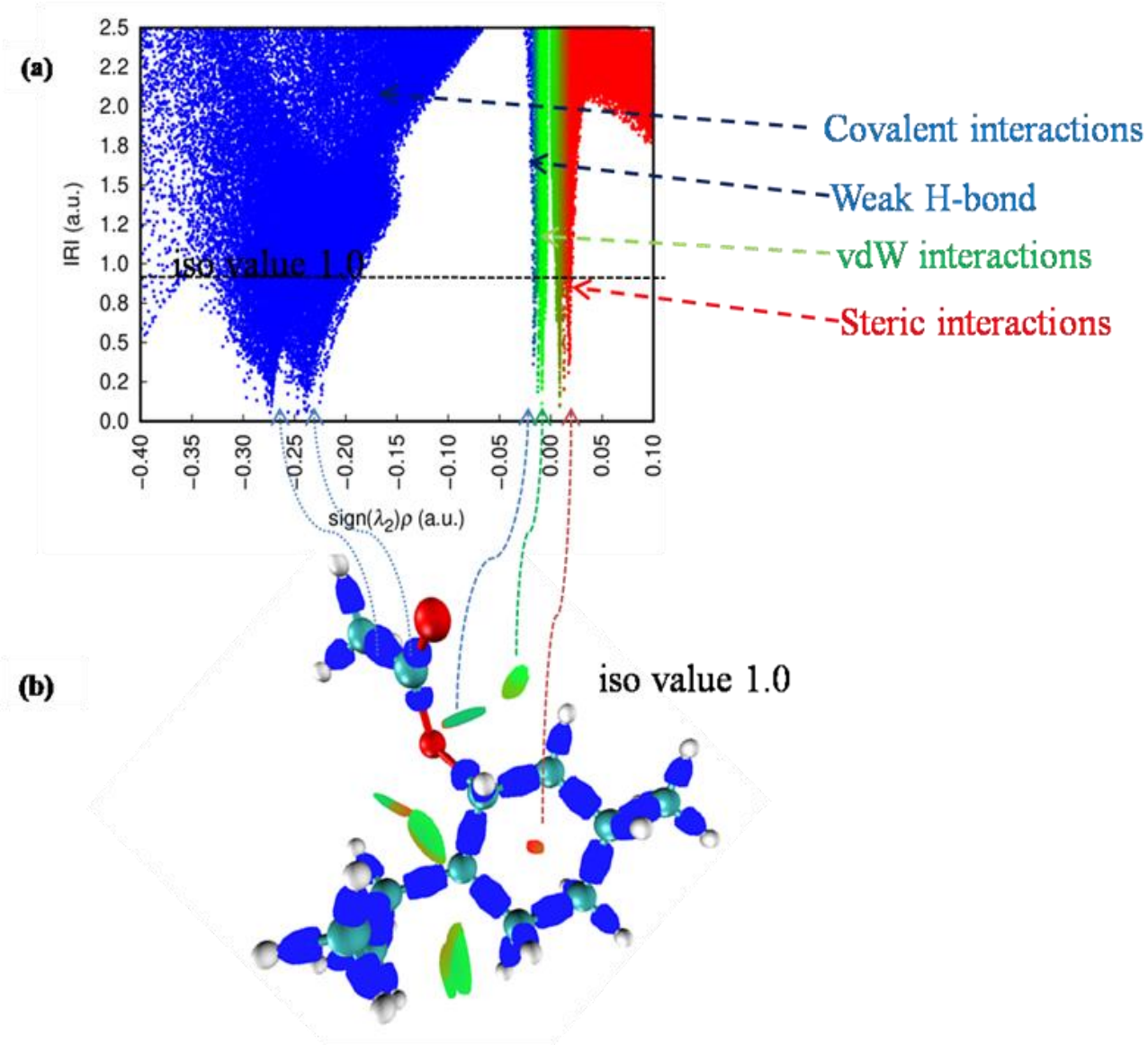

Figure 14. (a) IRI isosurface map and (b) Scatter Plot of IRI versus the electron density multiplied by the sign of the second Hessian eigen value of RMA at iso value 1.0 (dashed horizontal line in map)

Light blue areas suggest the presence of H−bonds as we seen in the NCI analysis section. Red regions highlight zones of steric interaction, where the close approach of bulky groups leads to electron cloud overlap and repulsive forces occur.

3.6.4. *ELF and LOL analyses*

To understand the behavior of electrons on the molecular surface, we employed tools such as the ELF and LOL bump maps.

These tools provide insights into regions where electrons are most likely to be located around atoms. For instance, bump maps show broad or sharp peaks based on the electron density distribution, helping to identify electron pairs present on the molecule's surface [15, 18]. ELF and LOL both give similar information because they are based on how the electrons move. ELF focuses on where electron pairs are located, while LOL shows how tightly orbitals are grouped, especially in areas where orbitals overlap [39−41].

The contour planes were selected through chemically significant regions of RMA particularly across the cyclohexane ring and nearby functional groups. A specific plane passing through atoms H12···O36···H25 was chosen to visualize the electron localization through ELF and LOL, involved in intra−molecular C–H···O interactions. Although the overall symmetry of RMA is C1 due to substituents and chirality, the electron density near these atoms exhibits local pseudo−C_2 symmetry, which aids in recognizing weak yet directional non−covalent contacts [42]. The ELF and LOL distributions along this plane are represented in 2D structured Figure 15, with spatial dimensions in Bohr units.

The ELF map ranges from 0 to 1, where lower values (below 0.5) mean electrons are more spread out or delocalized [43, 44]. LOL values above 0.5 show areas where electrons are more concentrated, often in C−H···O bonds or near the center of atoms [45, 46]. The blue areas show where there is more number of electrons around hydrogen atoms (H12 and H25) and oxygen atom O36 in ELF. Red and orange areas highlight important chemical regions, usually found around hydrogen atoms of the C−H···O H−bond.

The hydrogen atoms in LOL appear white in the map, which means the electron density is very high above the top limit of the color scale (0.80).Thus, as discussed earlier from the NMR and AIM analysis, there is clear evidence of an intra−molecular bond of the type C–H···O. The movement of electrons from the donor (C–H) to the acceptor (C=O) is clearly visible in the ELF and LOL maps.

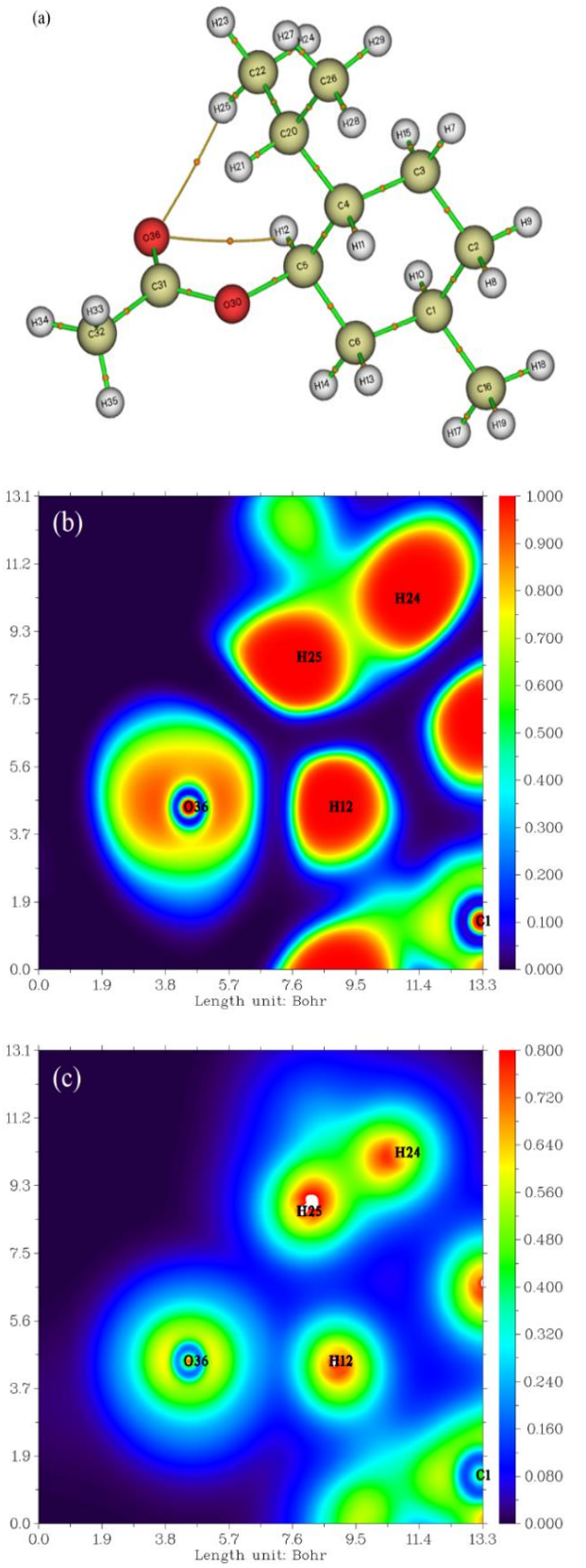

Figure 15. (a) Selected plane for visualization. Plotting maps of (b) ELF and (c) LOL for the atoms H12···O36···H25 of RMA. The color scale from black to red (0 to 1.0) represents increasing electron concentration. The dashed line indicates the bond between the hydrogen atom and the acceptor oxygen atom

4. Conclusions

The intra−molecular C–H···O bonded chair conformer of (R)−(−)−Menthyl Acetate has been proposed based on DFT and QT−AIM analyses. Calculations at the B3LYP/6−311+G(d,p) level show excellent agreement with experimental IR, Raman frequencies and ^{1}H NMR data particularly the observed downfield chemical shift at δ 4.68 ppm confirming the influence of the C–H···O bond. The computed chemical shift of δ 4.78 ppm for the proton in C–H···O bond is in excellent agreement with the experimental value.

Further, the presence of multiplets in the ^{1}H NMR spectrum near δ 1.87 ppm confirms significant steric hindrance due to the protons in the cyclohexane ring and isopropyl group, thereby restricting conformational flexibility.

The computed H···O separation of 2.351 Å, notably shorter than the sum of the van der Waals radii of H and O atoms, further supports the presence of this intra−molecular bond. ECD studies, combined with TD−DFT calculations, show a strong positive Cotton effect at 232 nm and is correlated with the $n\rightarrow\pi^*$ transition, thereby reinforcing the above C–H···O bonded conformation.

The close correspondence between the calculated ECD band at 214 nm and the experimental band at 232 nm strengthens the proposed chair conformation model. NBO analysis highlights significant charge delocalization, as evidenced by the $n(2)O\rightarrow\pi^*(C=O)$ interaction with a stabilization energy of ~47 kcal mol^{-1}. Visualization through ELF and LOL maps provide the spatial electron density distribution around the C–H···O bonding. FMO analysis indicates a large HOMO–LUMO gap (~7.6 eV), consistent with high electronic stability for the above said conformer. Combined topological and visual mapping (AIM, NCI, IRI) clearly differentiate weak non−covalent from covalent forces and demonstrates the relative strengths of van der Waals, steric, and C–H···O bonding in the conformer stability.

Authors Contribution

The authors thank the Director, USIC at Karnatak University, Dharwad for ATR−FTIR, UV−Vis and CD spectrometer commissioned under DST−funded PURSE−II Program and 400 MHz FT−NMR spectrometer under DST SAIF program. Kiran Gadivaddar gratefully acknowledged Karnatak University, Dharwad, for awarding a University Research Studentship.

Availability of data and materials

The datasets used and/or analyzed during the current study are available from the corresponding author upon reasonable request

Conflict of interests

The authors declare that there is no conflict of interests regarding the publication of this article.

References

[1] Yanlong Chen, Zicheng Lu, Gongke Li and Yuling Hu; β−Cyclodextrin porous polymers with three−dimensional chiral channels for separation of polar racemates, J. Chromatogr. A, 1626 (2020). DOI: https://doi.org/10.1016/j.chroma.2020.461341.

[2] Gretta C., M'bitsi−Ibouily, T Marimuthu, P Kumar, Y E Choonara, Lisa C du Toit, PriyamvadaPradeep,GModi, V Pillay; Synthesis, characterisation and in vitro permeation, dissolution and cytotoxic evaluation of ruthenium(II)−ligandedsulpiride and amino alcohol, Sci. Rep., 9 (2019). DOI: https://doi.org/10.1038/s41598-019-40538-1.

[3] P. Bolze, G. Dickmeiss and K. A. Jørgensen; Organocatalytic asymmetric synthesis of 5−(trialkylsilyl)cyclohex−2−enones and the transformation into useful building blocks, Org. Lett., 10(17), pp. 3753–3756 (2008). DOI: https://doi.org/10.1021/ol801392d.

[4] M. Egan, É. M. Connors, Z. Anwar and J. J. Walsh; Nature's treatment for irritable bowel syndrome: Studies on the isolation of (–)−menthol from peppermint oil and its conversion to (–)−menthyl acetate, J. Chem. Educ., 92(10), pp. 1736–1740 (2015). DOI: https://doi.org/10.1021/ed5007037.

[5] S. K. Srivastava, A. Ahmad, K. V. Syamsunder, K. K. Aggarwal and S. P. S. Khanuja; Essential oil composition of *Callistemon viminalis* leaves from India, FlavourFragr. J., 18(5) (2003). DOI: https://doi.org/10.1002/ffj.1143.

[6] Frisch, M. J., Trucks, G. W., Schlegel, H. B., Scuseria, G. E., Robb, M. A., Cheeseman, J. R., Scalmani, G., Barone, V., Petersson, G. A., Nakatsuji, H., Caricato, M., Li, X., Hratchian, H. P., Izmaylov, A. F., Bloino, J., Zheng, G., Sonnenberg, J. L., Hada, M., Ehara, M., Toyota, K., Fukuda, R., Hasegawa, J., Ishida, M., Nakajima, T., Honda, Y., Kitao, O., Nakai, H., Vreven, T., Montgomery, J. A., Peralta, J. E., Ogliaro, F., Bearpark, M., Heyd, J. J., Brothers, E., Kudin, K. N., Staroverov, V. N., Keith, T., Kobayashi, R., Normand, J., Raghavachari, K., Rendell, A., Burant, J. C., Iyengar, S. S., Tomasi, J., Cossi, M., Rega, N., Millam, J. M., Klene, M., Knox, J. E., Cross, J. B., Bakken, V., Adamo, C., Jaramillo, J., Gomperts, R., Stratmann, R. E., Yazyev, O., Austin, A. J., Cammi, R., Pomelli, C., Ochterski, J. W., Martin, R. L., Morokuma, K., Zakrzewski, V. G., Voth, G. A., Salvador, P., Dannenberg, J. J., Dapprich, S., Daniels, A. D., Farkas, O., Foresman, J. B., Ortiz, J. V., & Fox, D. J.

(2013). *Gaussian 09, Revision D.01*. Gaussian, Inc., Wallingford, CT.

[7] J. P. Merrick, D. Moran and L. Radom; An evaluation of harmonic vibrational frequency scale factors, J. Phys. Chem. A, 111(45), pp. 11683–11700 (2007). DOI: https://doi.org/10.1021/jp073974n.

[8] M. H. Jamróz; Vibrational energy distribution analysis VEDA 4, Spectrochim. Acta A Mol. Biomol. Spectrosc., 114, pp. 220–230 (2013).

[9] F. Weinhold and R. A. Klein; What is a hydrogen bond? Mutually consistent theoretical and experimental criteria for characterizing H−bonding interactions, Mol. Phys., 110(5), pp. 565–579 (2012). DOI: https://doi.org/10.1080/00268976.2012.661478

[10] M. D. Prabhu, J. TonannavarYenagi, V. Kamat and J. Tonannavar; XRD structure and vibrational analysis of DL−β−Leucine, as aided by DFT tetramer model and characterized by NBO, AIM and NCI calculations, J. Mol. Struct., 1218 (2020). DOI: https://doi.org/10.1016/j.molstruc.2020.128495

[11] R. P. Kavali, J. Tonannavar, J. Bhovi and J. Tonannavar; Study of O–H•••O bonded−cyclic dimer for 2,5−dihydroxyterephthalic acid as aided by MD, DFT calculations and IR, Raman, NMR spectroscopy, J. Mol. Struct., 1264 (2022). DOI: https://doi.org/10.1016/j.molstruc.2022.133174

[12] L. Pallavi, J. Tonannavar and J. Tonannavar; Molecular dynamics simulation, DFT calculations and vibrational spectroscopic study of N–H•••O bound dimer models for DL−β−phenylalanine and 3−amino−3−(4−chlorophenyl)propionic acid, J. Mol. Liq., 352, 11846 (2022). DOI: https://doi.org/10.1016/j.molliq.2022.118746

[13] S. S. Malaganvi, J. TonannavarYenagi and J. Tonannavar; Spectroscopic and electronic structure characterization of hydrogen bonding in 2−Bromohydroquinone, J. Mol. Struct., 1181, pp. 71–82 (2019). DOI: https://doi.org/10.1016/j.molstruc.2018.12.063

[14] J. Bhovi, J. R. Tonannavar and J. J. Tonannavar; A combined experimental, molecular dynamics, DFT, NBO and AIM analyses of O–H•••O cyclic dimer model of hippuric acid, IOSR J. Appl. Chem., 17(2), pp. 54–68 (2025). DOI: https://doi.org/10.9790/4861−1702035468

[15] R. F. W. Bader; Atoms in Molecules − A Quantum Theory, Oxford University Press, Oxford, (1990).

[16] W. Humphrey, A. Dalke and K. Schulten; VMD: Visual molecular dynamics, J. Mol. Graph., 14(1) (1996). DOI: https://doi.org/10.1016/0263−7855(96)00018−5

[17] Tian Lu; A comprehensive electron wavefunction analysis toolbox for chemists, Multiwfn, J. Chem. Phys., 161(8) (2024). DOI: https://doi.org/10.1063/5.0216272

[18] M. Medimagh, M. Y. Mhiri, A. A. Alharbi and A. A. Alghamdi; Investigations on the non−covalent interactions, drug−likeness, molecular docking and chemical properties of 1,1,4,7,7−pentamethyldiethylenetriammonium trinitrate by density−functional theory, J. King Saud Univ. Sci., 35(4) (2023). DOI: https://doi.org/10.1016/j.jksus.2023.102645

[19] Tian Lu and Q. Chen; Interaction region indicator: A simple real space function clearly revealing both chemical bonds and weak interactions, Chem. Methods, 1(5), pp. 231–239 (2021). DOI: https://doi.org/10.1002/cmtd.202100007

[20] S. Tanga, D. Z. Yuan, Z. Lia, Y. Guo and X. Yin; 5−Hydroxysalicylic acid investigated by terahertz spectroscopy and density functional theory, Quim. Nova, 45(8), pp. 913–920 (2022). DOI: https://doi.org/10.21577/0100−4042.20170896

[21] T. Egawa, M. Sakamoto, H. Takeuchi and S. Konaka; Structural determination of menthol and isomenthol, a minty compound and its nonminty isomer, by means of gas electron diffraction augmented by theoretical calculations, J. Phys. Chem. A, 107(15), pp. 2757–2762 (2003). DOI: https://doi.org/10.1021/jp022163a

[22] G. R. Desiraju and T. Steiner; The Weak Hydrogen Bond: In Structural Chemistry and Biology, Oxford University Press, Oxford, (1999).

[23] Raymond J. Abraham, Mark A. Warne and Lee Griffiths; Proton chemical shifts in NMR. Part 12.1 Steric, electric field and conformational effects in acyclic and cyclic ethers, J. Chem. Soc., Perkin Trans. 2, pp. 1751–1757 (1998). DOI: https://doi.org/10.1039/A802950D

[24] H. Günther; NMR Spectroscopy: Basic Principles, Concepts and Applications in Chemistry, 3rd ed., Wiley−VCH, (2013).

[25] W. Kemp; Organic Spectroscopy, 3rd ed., Palgrave, Basingstoke and New York, (1991). DOI: https://doi.org/10.1007/978−1−349−15203−2

[26] R. M. Silverstein, F. X. Webster and D. J. Kiemle; Spectrometric Identification of Organic Compounds, 8th ed., John Wiley & Sons, (2015).

[27] Z. Zeng, G. Kociok−Köhn, T. J. Woodman, M. G. Rowan and I. S. Blagbrough; The 1H NMR spectroscopic effect of steric compression is found in [3.3.1] oxa− and azabicycles and their analogues, ACS Omega, (2021).
DOI: https://doi.org/10.1021/acsomega.1c01093

[28] G. Zhu, Z. Xiao, R. Zhou, G. Zhu and Y. Niu; Kinetics and release characteristics of menthyl acetate from its β−cyclodextrin inclusion complex by thermogravimetric analysis, J. Incl. Phenom. Macrocycl. Chem., 84(3–4), pp. 219–224 (2016).
DOI: https://doi.org/10.1007/s10847−016−0599−y

[29] Datta, S., Sett, P., Chowdhury, J., Ghosh, M., and Mallick, P. K.; Excited Electronic States and Raman Spectra of 2-Benzoylpyridine. *Applied Spectroscopy*, 67(12), 1447–1462 (2013).
DOI: https://doi.org/10.1366/13-07166

[30] D. K. Pandey and P. S. Yadav; Ab-Initio Study of Structural and Electronic Properties of ZnxTey (x + y = 2 to 5) Nanoclusters, Advanced Science, Engineering and Medicine Vol. 12, 930 – 938 (2020).
DOI: https://doi.org/10.1166/asem.2020.2634

[31] P. Verma, A. Srivastava, P. Tandon and M. R. Shimpi; Experimental and quantum chemical studies of nicotinamide−oxalic acid salt: Hydrogen bonding, AIM and NBO analysis, Front. Chem., 10, 855132 (2022).
DOI: https://doi.org/10.3389/fchem.2022.855132

[32] M. Abuelela, M. A. Bedair, W. M. Zoghaib, L. D. Wilson and T. A. Mohamed; Molecular structure and mild steel/HCl corrosion inhibition of 4,5−dicyanoimidazole: Vibrational, electrochemical and quantum mechanical calculations, J. Mol. Struct., 1230, p. 129647 (2021).
DOI: https://doi.org/10.1016/j.molstruc.2020.129647

[33] J. Yenagi, A. Shettar and J. Tonannavar; On the anomalous vibration spectra and OH···N bond dictated structure of 3−fluoroisonicotinic acid, Vib. Spectrosc., 63, pp. 342–349 (2012).
DOI: https://doi.org/10.1016/j.vibspec.2012.08.005

[34] Mithil Kotyagol, J. Tonannavar and JayashreeTonannavar; Computational and Experimental Studies on Double H−Bonded Zwitterion Dimer Model for L−2−Aminoadipic Acid, Asian J. Chem., 37, pp. 1431–1448 (2025).
DOI: https://doi.org/10.14233/ajchem.2025.33831

[35] M. Khalid, A. Hussain, A. A. Alhazmi, I. H. Jehangir and S. M. Alshehri; Exploration of noncovalent interactions, chemical reactivity and nonlinear optical properties of piperidone derivatives: A concise theoretical approach, ACS Omega, 5(22), pp. 13236–13249 (2020).
DOI: https://doi.org/10.1021/acsomega.0c01273

[36] Ramanna P., J. Tonannavar and J. Tonannavar; Study of H−bonded cyclic dimer of organic linker 5−bromoisophthalic acid by DFT and vibrational spectroscopy, J. Mol. Struct., 1241 (2021).
DOI: https://doi.org/10.1016/j.molstruc.2021.130613

[37] J. Bhovi, J. Tonannavar and J. J. Tonannavar; IR, Raman spectroscopic, DFT, AIM and NCI characterization of O–H•••O/π•••π bonds in dimer and trimer species as computed from MD simulations in water for protocatechuic acid, J. Mol. Struct., 1299, p. 137077 (2024).
DOI: https://doi.org/10.1016/j.molstruc.2023.137077

[38] G. Saleh, C. Gatti and L. Lo Presti; Non−covalent interaction via the reduced density gradient: Independent atom model vs experimental multipolar electron densities, Comput. Theor. Chem., 998, pp. 148–163 (2012).
DOI: https://doi.org/10.1016/j.comptc.2012.07.014

[39] F. Akman, A. Demirpolat, A. S. Kazachenko, N. Issaoui and O. Al−Dossary; NCI−RDG studies of the binary mixture of water and essential oil of Phlomisbruguieri, (2023).

[40] S. B. Radder, R. Melavanki, U. Radder, S. M. Hiremath, R. Kusanur and S. S. Khemalapure; Synthesis, spectroscopic (FT−IR, FT−Raman, NMR), reactivity (ELF, LOL and Fukui) and docking studies on 3−(2-hydroxy−3-methoxy−phenyl)−1−(3−nitro−phenyl)−propenone by experimental and DFT methods, J. Mol. Struct., 1255, p. 132443 (2022).
DOI: https://doi.org/10.1016/j.molstruc.2022.132443

[41] J. D. D. Tarika, X. D. D. Dexlin, S. Madhankumar, D. D. Jayanthi and T. J. Beaula; Tuning the computational evaluation of spectroscopic, ELF, LOL, NCI analysis and molecular docking of novel anti−COVID−19 molecule 4−dimethylamino pyridinium 3,5−dichlorosalicylate, Spectrochim. Acta A Mol. Biomol. Spectrosc., 259, p. 119907 (2021).
DOI: https://doi.org/10.1016/j.saa.2021.119907

[42] D. Becke and K. E. Edgecombe; A simple measure of electron localization in atomic and molecular systems, J. Chem. Phys., 92(9), pp. 5397–5403 (1990).
DOI: https://doi.org/10.1063/1.458517

[43] K. Arulaabaranam, S. Muthu, G. Mani and A. S. Ben Geoffrey; Speculative assessment, molecular composition, PDOS, topology exploration (ELF, LOL, RDG), ligand−protein interactions, Heliyon, 7(5), p. e07061 (2021).
DOI: https://doi.org/10.1016/j.heliyon.2021.e07061

[44] F. R. B., S. Muthu, J. Christian, C. Susan and M. Raja; Spectroscopic (FT−IR, FT−Raman) investigation, topology (ESP, ELF, LOL) analyses, charge transfer excitation and molecular docking (dengue, HCV) studies on ribavirin, Chem. Data Collect., 17–18, pp. 236–250 (2018).
DOI: https://doi.org/10.1016/j.cdc.2018.09.003

[45] F. Fuster, A. Sevin and B. Silvi; Topological analysis of the electron localization function (ELF) applied to the electrophilic aromatic substitution, J. Theor. Comput. Chem., 2(1), pp. 852–858 (2000).
DOI: https://doi.org/10.1021/jp992783k

[46] F. Bardak, H. T. Flakus, A. Atac, N. Issaoui, H. Ghalla and S. Antonia; Experimental FTIR and FT−Raman and theoretical studies on the molecular structures of monomer and dimer of 3−thiopheneacrylic acid, J. Mol. Struct., 1135 (2017).
DOI: https://doi.org/10.1016/j.molstruc.2017.01.074

[47] Y. R. Sharma; Elementary Organic Spectroscopy, ed. 1, S. Chand & Co. Pvt. Ltd., New Delhi, (1980).

[48] S. H. Crouch,D.A. Skoog and F.J. Holler; Principles of Instrumental Analysis, edn. 7, Cengage Learning, (2017)